

# EchoVLM: Dynamic Mixture-of-Experts Vision-Language Model for Universal Ultrasound Intelligence

Chaoyin She<sup>1\*</sup>, Ruifang Lu<sup>2\*</sup>, Lida Chen<sup>2†</sup>, Wei Wang<sup>2†</sup>, Qinghua Huang<sup>1†</sup>

<sup>1</sup>Northwestern Polytechnical University

<sup>2</sup>The First Affiliated Hospital of Sun Yat-Sen University

## Abstract

Ultrasound imaging has become the preferred imaging modality for early cancer screening due to its advantages of non-ionizing radiation, low cost, and real-time imaging capabilities. However, conventional ultrasound diagnosis heavily relies on physician expertise, presenting challenges of high subjectivity and low diagnostic efficiency. Vision-language models (VLMs) offer promising solutions for this issue, but existing general-purpose models demonstrate limited knowledge in ultrasound medical tasks, with poor generalization in multi-organ lesion recognition and low efficiency across multi-task diagnostics. To address these limitations, we propose EchoVLM, a vision-language model specifically designed for ultrasound medical imaging. The model employs a Mixture of Experts (MoE) architecture trained on data spanning seven anatomical regions. This design enables the model to perform multiple tasks, including ultrasound report generation, diagnosis and visual question-answering (VQA). The experimental results demonstrated that EchoVLM achieved significant improvements of 10.15 and 4.77 points in BLEU-1 scores and ROUGE-1 scores respectively compared to Qwen2-VL on the ultrasound report generation task. These findings suggest that EchoVLM has substantial potential to enhance diagnostic accuracy in ultrasound imaging, thereby providing a viable technical solution for future clinical applications. Source code and model weights are available at <https://github.com/Asunatan/EchoVLM>.

## Introduction

Ultrasound imaging is now a key clinical diagnostic tool, thanks to its advantages such as no ionizing radiation, cost-effectiveness, and real-time visualization. Due to these features, it is indispensable for early cancer detection, prenatal care, and dynamic assessment of organs like the thyroid, breast, liver, kidneys, cardiovascular and heart systems. However, traditional ultrasound diagnosis is subject to the professional expertise of radiologists. This reliance can lead to differing interpretations among observers and delays in diagnosis and treatment efficiency due to manual interpretation. Visual language models (VLMs) have achieved re-

\*These authors contributed equally.

† Corresponding author

Copyright © 2026, Association for the Advancement of Artificial Intelligence (www.aaai.org). All rights reserved.

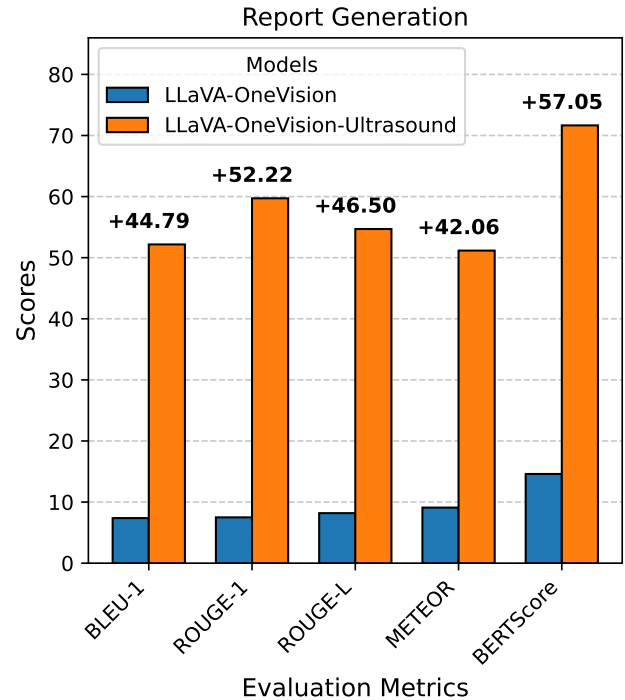


Figure 1: Generic vs. ultrasound-specialized LLaVA-OneVision performance comparison.

markable advancements in multimodal perception and contextual understanding, significantly impacting medical image analysis across diverse modalities. However, applying these models to ultrasound diagnosis presents domain-specific challenges. For instance, the scarcity of ultrasound-specific expertise and the necessity to account for organ-specific anatomical variations pose significant hurdles. As demonstrated in Figure 1, our preliminary experiments with LLaVA-OneVision (Li et al. 2024) highlight the imperative need for specialized VLMs tailored to ultrasonography. The performance disparities revealed in this comparison underscore the limitations of generic models in capturing the nuanced characteristics inherent to ultrasound imaging. Such deficiencies hinder the seamless integration of multimodal

learning frameworks into clinical ultrasound workflows, where precision and anatomical specificity are paramount.

To address this critical gap, we introduce EchoVLM, the first ten-billion-parameter universal ultrasound-specialized VLM. Our framework is built upon three core innovations: First, we have curated the largest multi-organ ultrasound dataset to date, comprising 208,941 clinical cases and 1.47 million key imaging sections from 15 hospitals, spanning seven major organ systems: thyroid, breast, liver, kidney, gynecology, vessel, and heart. This comprehensive dataset ensures broad anatomical coverage for robust model training. Second, inspired by Self-Instruct (Wang et al. 2023), we propose a few-shot prompting mechanism with expert validation, enabling the construction of a multi-task instruction-tuning data generation pipeline. This approach systematically synthesizes diverse diagnostic scenarios while maintaining clinical accuracy through expert oversight. Third, we integrate a Dual-path MoE module with a dynamic routing mechanism, enhancing the model’s adaptability to the heterogeneous and complex nature of ultrasound imaging tasks. This architecture allows task-specific expert subnetworks to specialize in distinct diagnostic domains, improving both efficiency and precision.

In summary, our contributions are as follows:

- We pioneeringly propose the first universal ultrasound-specialized VLM, EchoVLM, which is specifically designed to address the challenges of ultrasound diagnosis.
- We have compiled a large-scale dataset from 15 hospitals, containing 208,941 cases and 1.47 million key imaging sections across seven major organ systems. Using this dataset, we have developed a multi-task instruction-tuning data generation pipeline for ultrasound.
- We incorporate a Dual-path MoE module into the EchoVLM model. The MoE module employs a dynamic routing mechanism, which significantly improves the model’s adaptability to the diverse and complex nature of ultrasound tasks.

## Related Work

The advent of large language models (LLMs) has catalyzed paradigm shifts in artificial intelligence research, particularly in natural language processing domains encompassing linguistic comprehension, generative capabilities, and text-centric task execution. Nevertheless, conventional unimodal LLM architectures exhibited intrinsic limitations in visual perception modalities, thereby constraining their applicability to real-world scenarios requiring cross-modal integration. To overcome this, researchers have proposed multi-level fusion mechanisms, including abstract layers (Radford et al. 2021; Vasu et al. 2024; Zhang et al. 2024a), semantic embedding layers (Liu et al. 2023; Lin et al. 2024a,b), and cross-attention layers (Li et al. 2023b; Alayrac et al. 2022), to achieve collaborative integration of visual and textual features. In this context, the BLIP series pioneered the use of cross-attention mechanisms for dynamic interaction between visual features and textual elements, while LLaVA introduced visual instruction tuning—a paradigm leveraging visual data to refine models’ perceptual capabilities through

fine-tuning. Subsequent developments further enhanced performance by expanding datasets (Liu et al. 2024a; Zhang et al. 2024c), improving image resolution (Liu et al. 2024b; Wang et al. 2024; Hong et al. 2024), incorporating multi-image and video understanding frameworks (Kar et al. 2024; Fan et al. 2024), optimizing projection layers (Li et al. 2026; Chen et al. 2025; Tong et al. 2024), and employing multiple visual encoders. Recent advancements emphasize fine-grained understanding, integrating object localization (e.g., bounding boxes) and segmentation masks to improve spatial and semantic precision (Guo et al. 2024; Zhang et al. 2024b).

Notably, recent studies have begun exploring VLM applications in medical domains, with LLaVA-Med (Li et al. 2023a) emerging as a representative framework. However, these systems demonstrate significant limitations in specialized clinical contexts, particularly exhibiting deficiencies in ultrasound-specific knowledge acquisition that hinder structured report generation. Furthermore, such approaches lack sufficient context length to effectively address multi-image scenarios prevalent in ultrasound imaging. To overcome these domain-specific challenges, this study proposes the development of a dedicated ultrasound-centric VLM architecture specifically optimized for diagnostic imaging workflows and medical terminology standardization in sonographic analysis.

## Method

### Data Collection and Instruction-Tuning Data Generation Pipeline

To develop a VLM tailored to the ultrasound imaging domain, we compiled a comprehensive dataset sourced from 15 hospitals. This dataset encompasses the seven major anatomical areas commonly assessed via ultrasound: the liver, kidney, thyroid, vascular system, gynecology, heart, and breast. To guarantee data quality, a strict data filtration protocol was implemented: (1) Image Filtering. When exporting images from hospital databases, only single-region images were selected to prevent multi-region confusion. Additionally, we manually removed images that lacked corresponding reports to ensure alignment between imaging data and clinical documentation. (2) Text Filtering. Manually screened and eliminated reports unrelated to the specific region and those lacking corresponding images. This bidirectional filtering yielded 208,941 cases containing 1.47 million key-frame ultrasound images.

Building upon this foundation, we established a structured pipeline for instruction-tuning data generation using a few-shot prompting strategy (see Figure 3). Medical experts were invited to develop 21 exemplar templates spanning diverse anatomical pathologies, with each template integrating three components designed to simulate real-world clinical processes: (1) Ultrasound descriptions: Detailed ultrasound findings documenting lesion location, size, morphology, echogenicity patterns, and other relevant features derived from image analysis. (2) Ultrasound diagnosis: Clinical summaries synthesizing key observational findings into standardized diagnostic statements. (3) Question-

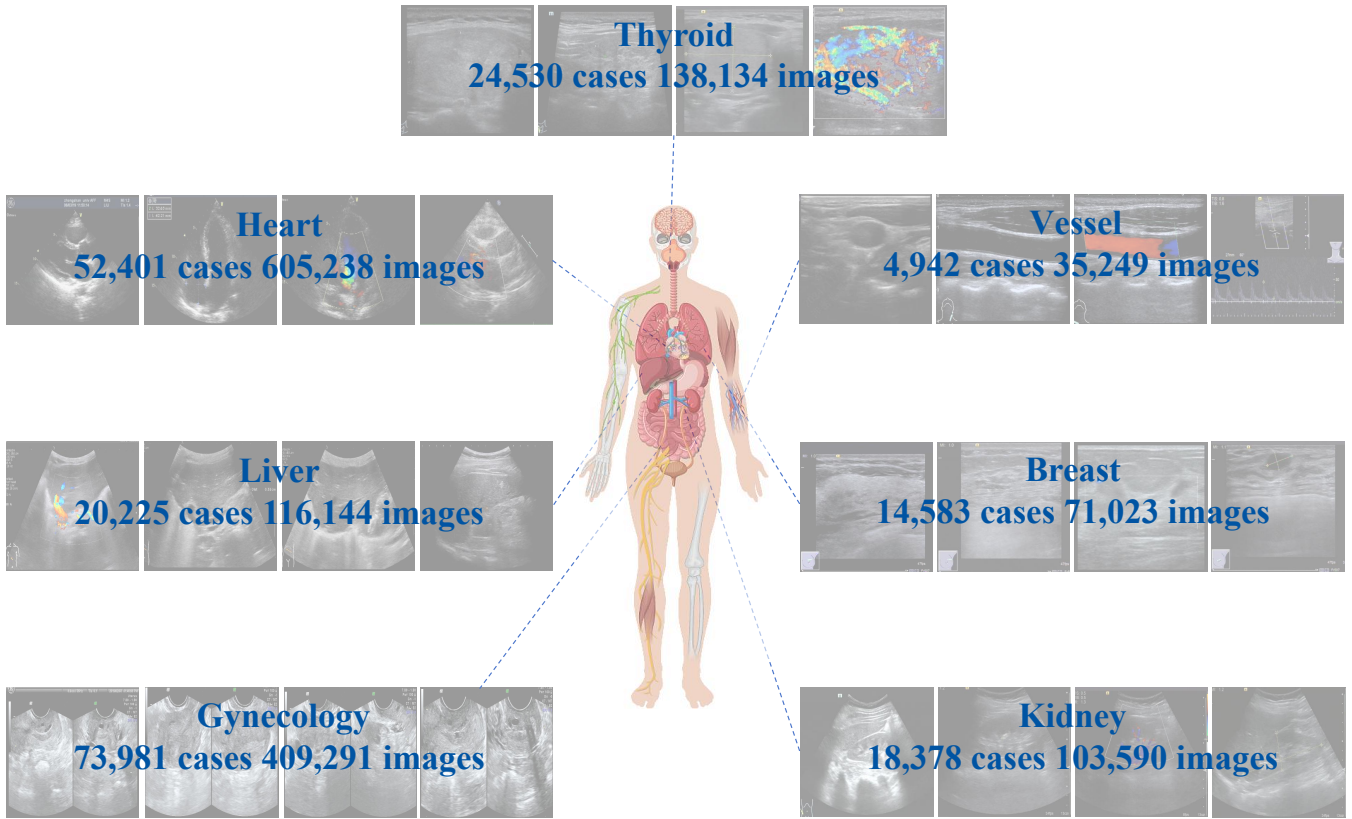


Figure 2: This multicenter ultrasound dataset encompasses seven anatomical regions with heterogeneous clinical cases, including thyroid, heart, vessel, liver, breast, and kidney ultrasound images.

answer pairs: Multidimensional question-answer sets including diagnostic interpretation, risk stratification, patient counseling, surveillance strategies, and treatment planning considerations.

Subsequently, templates were systematically classified into open-ended and closed-ended categories, with tailored prompting strategies designed for each type. For open-ended templates, models were instructed to generate both questions and answers by referencing the provided examples, while for closed-ended templates, models were tasked with generating diverse questions, with answers derived from real ultrasound reports and diagnoses to ensure clinical accuracy. To remove redundancy, the generated data were processed through ROUGE-L and Simhash-based deduplication pipelines. Furthermore, the open-ended subset underwent dual validation for accuracy: automated evaluation using a LLM and manual review of randomly sampled data by medical experts to ensure the quality of the generated content. This pipeline yielded a final dataset of 1.8 million instruction-tuning data pairs. Further details are provided in the Supplementary Materials.

### Architecture of EchoVLM

We propose EchoVLM, a vision-language model specifically engineered for ultrasound clinical analysis through targeted domain specialization of the Qwen2-VL founda-

tion model. Central to this architecture are two pre-trained modal components: the Qwen-2 language model and a modified CLIP-based visual encoder, which are synergistically combined through a bridging mechanism. This integration is achieved via a computation-efficient Multilayer Perceptron (MLP) projection layer specifically designed to enable precise cross-modal alignment between the textual and visual representations. Rather than naively fine-tuning these components on ultrasound corpora, we introduce a Dual-path MoE mechanism that injects domain knowledge while shielding pre-existing representations from destructive updates.

For the visual encoder, any RGB ultrasound frame  $v \in \mathbb{R}^{H \times W \times 3}$  are encoded by a modified CLIP encoder to generate a discrete visual token representations  $V = [v_1, v_2, \dots, v_m] \in \mathbb{R}^{M \times C}$ . Here,  $M = HW/14^2$  denotes the number of visual tokens derived from the original spatial resolution  $H \times W$ . These visual tokens are subsequently transformed into the dimensional space of the Qwen-2 via a MLP projector  $f(\cdot)$ , yielding dimensionally-mapped visual embeddings  $V \in \mathbb{R}^{M \times D}$ . Simultaneously, textual inputs undergo parallel processing: the input prompts are first tokenized and then embedded through the word-embedding layer  $w(\cdot)$ , generating the textual token sequence  $T = [t_1, t_2, \dots, t_N] \in \mathbb{R}^{N \times D}$ , where  $N$  represents the number of text tokens determined by the input prompt length. The

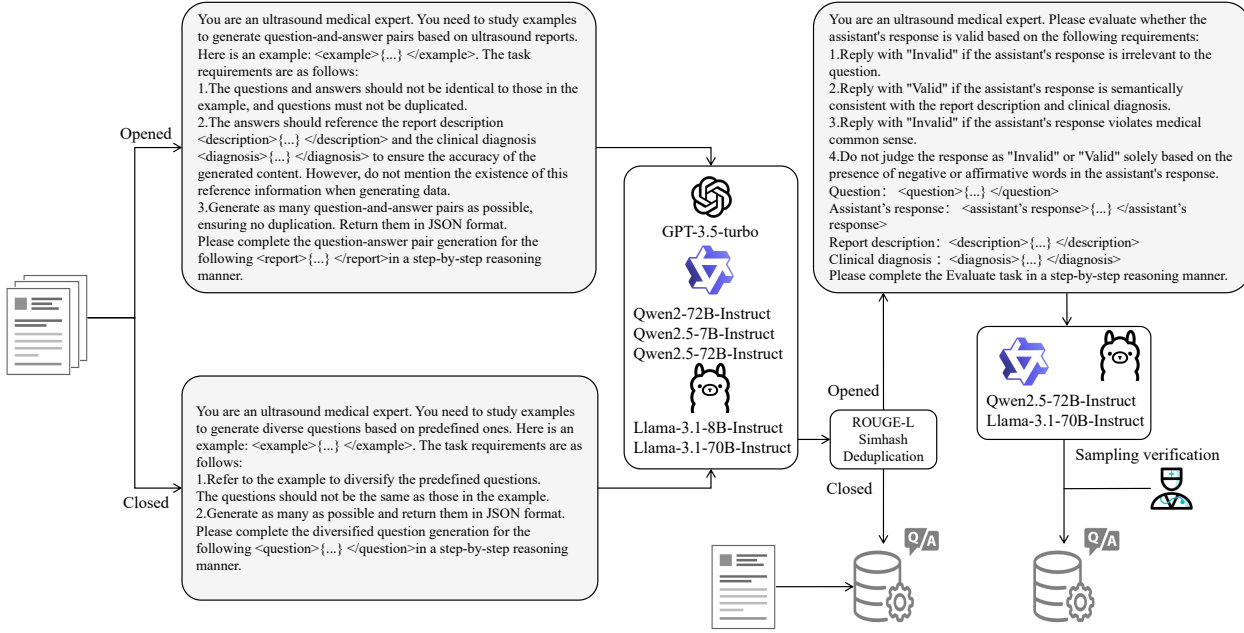


Figure 3: Overview of the proposed instruction-tuning data generation pipeline for ultrasound domain knowledge. The framework systematically produces and verifies ultrasound-oriented question-answer pairs by categorizing prompt templates into open-ended and closed-ended classes, ensuring both diversity and clinical fidelity.

Usage	images	reports	instruction samples
Stage I	1.47M	208,491	-
Stage II	1.47M	208,491	1.8M
Test	27,577	3000	-

Table 1: Data usage per stage: Stage I uses 1.47M images and 208,491 reports; Stage II adds 1.8M instruction samples; The held-out test set contains 27 577 images and 3 000 reports.

concatenated representation  $X_0 = [V; T] \in \mathbb{R}^{(M+N) \times D}$  is subsequently fed into the LLM which comprises multiple Transformer blocks. Each layer contains multi-head self-attention (MSA), layer-norm (LN), residual pathways, and a Dual-path MoE block. Its processing flow can be expressed as:

$$X'_i = \text{MSA}(\text{LN}(X_{i-1})) + X_{i-1}, \quad i = 1, \dots, L \quad (1)$$

$$X_i = \text{Dual-path MoE}(\text{LN}(X'_i)) + X'_i, \quad i = 1, \dots, L \quad (2)$$

## Dual-path MoE

Structurally, the Dual-path MoE layer comprises two complementary sets of experts. First, a static expert is instantiated by copying the original Qwen2 Feed-Forward Network (FFN) and immediately frozen; its parameters therefore act as a resilient anchor that conserves generic semantic capacity. Second, a battery of active experts is appended and trained. Within this group we further distinguish (1) a shared expert ( $S$ ) that processes every token, thereby sustaining a

Anatomical	Metric↑	LLaVA-OneVision (7B)	Qwen2-VL (7B)	LLaVA-OneVision-Ultrasonnd (7B)	Qwen2-VL-Ultrasonnd (7B)	EchoVLM(11B)
Breast	BLEU-1	8.36	8.92	44.61	41.74	50.76
	ROUGE-1	8.18	12.61	58.82	60.04	64.38
	ROUGE-L	9.22	9.71	47.22	49.94	55.21
	METEOR	9.46	8.93	46.27	43.52	50.14
	BERTScore	15.69	19.22	70.86	72.24	73.00
Gynecology	BLEU-1	6.87	6.62	40.90	42.67	52.52
	ROUGE-1	7.72	9.78	53.78	55.88	59.19
	ROUGE-L	7.88	8.11	43.51	44.22	51.64
	METEOR	9.49	8.51	42.67	44.32	52.76
	BERTScore	12.33	13.57	65.96	65.88	67.65
Heart	BLEU-1	10.55	6.77	71.47	68.12	76.48
	ROUGE-1	10.77	9.47	69.97	71.81	78.18
	ROUGE-L	8.99	7.12	73.15	73.04	80.64
	METEOR	8.66	5.99	69.03	63.48	70.73
	BERTScore	21.54	19.24	89.39	87.85	89.80
Kidney	BLEU-1	5.83	5.70	45.69	37.16	59.23
	ROUGE-1	5.44	7.28	58.23	47.13	65.78
	ROUGE-L	7.40	7.48	49.17	38.02	57.14
	METEOR	8.29	7.36	48.20	36.33	59.78
	BERTScore	13.93	14.61	70.23	62.67	75.89
Liver	BLEU-1	7.70	6.43	48.68	40.48	58.01
	ROUGE-1	6.94	8.85	59.21	51.93	67.06
	ROUGE-L	9.01	8.37	54.36	46.78	62.40
	METEOR	9.93	8.28	50.95	41.54	58.44
	BERTScore	14.27	14.37	72.23	65.98	75.68
Vessel	BLEU-1	3.20	3.39	43.50	37.62	29.54
	ROUGE-1	6.21	6.85	61.22	60.63	38.15
	ROUGE-L	4.36	4.52	54.49	55.38	32.29
	METEOR	6.16	4.91	52.43	46.50	30.38
	BERTScore	8.34	7.76	68.99	70.01	48.07
Thyroid	BLEU-1	7.10	7.13	33.44	38.25	50.55
	ROUGE-1	6.72	11.11	42.89	51.03	59.10
	ROUGE-L	8.38	8.79	33.89	41.00	51.16
	METEOR	8.98	8.60	31.32	37.63	49.87
	BERTScore	14.52	18.82	61.15	66.59	69.54
Average	BLEU-1	7.09	6.42	46.90	43.72	53.87
	ROUGE-1	7.43	9.42	57.73	56.92	61.69
	ROUGE-L	7.89	7.73	50.83	49.77	55.78
	METEOR	8.71	7.51	48.70	44.76	53.16
	BERTScore	14.37	15.37	71.26	70.17	71.38

Table 2: Report Generation Comparison.

universal ultrasound representation, and (2) a cohort of routing experts ( $E$ ) that are sparsely activated via a top-2 gating function conditioned on token-level features.

$$Y = \alpha \text{FFN}(X) + (1 - \alpha) \left[ \lambda S(X) + \sum_{i=1}^k g_i(X) E_i(\text{TopK}(X)) \right] \quad (3)$$

$$g_i(X) = \frac{e^{f_i(X)}}{\sum_{j=1}^k e^{f_j(X)}} \quad (4)$$

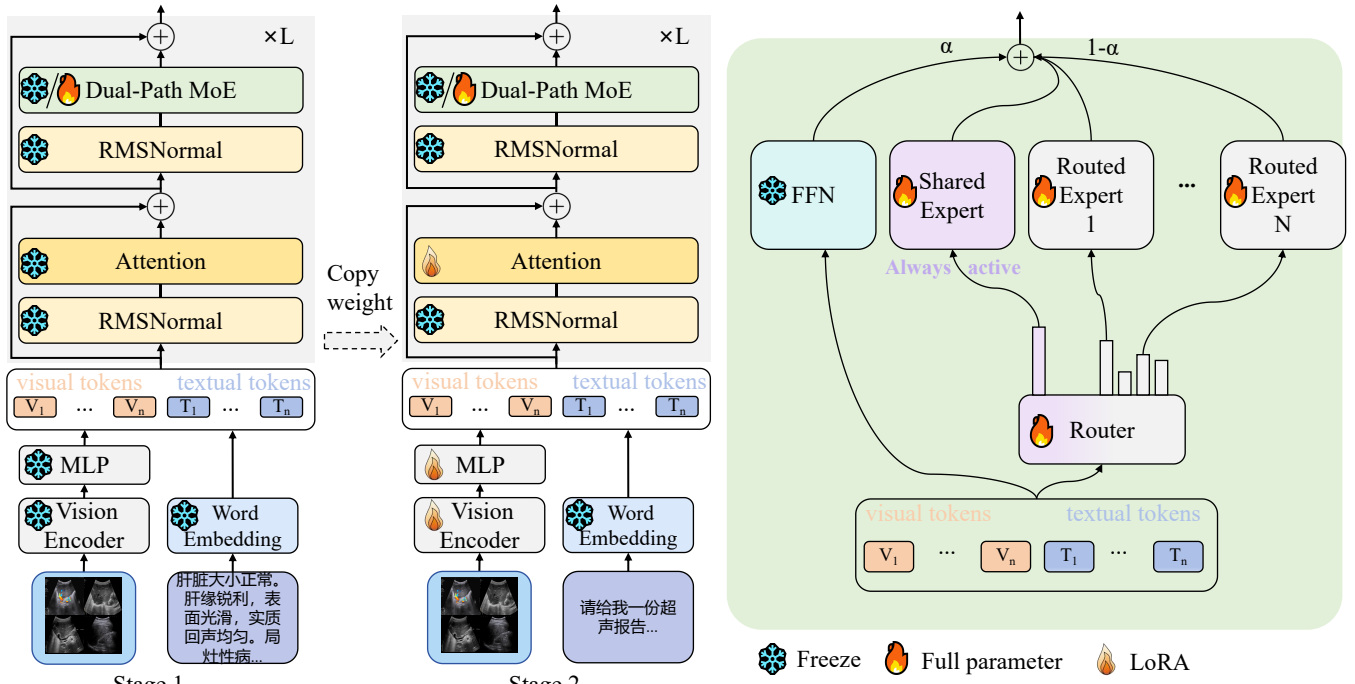


Figure 4: Architectural overview of EchoVLM.

Anatomical	Metric↑	LLaVA-OneVision (7B)	Qwen2-VL (7B)	LLaVA-OneVision-Ultrasound (7B)	Qwen2-VL-Ultrasound (7B)	EchoVLM
Breast	BLEU-1	7.73	10.40	64.25	56.22	<b>71.36</b>
	ROUGE-1	15.97	19.93	74.69	77.17	<b>80.77</b>
	ROUGE-L	10.38	13.50	66.47	70.63	<b>76.04</b>
	METEOR	17.99	21.16	72.38	71.42	<b>74.99</b>
	BERTScore	29.00	31.41	75.78	78.37	<b>81.68</b>
Gynecology	BLEU-1	6.01	9.98	30.16	40.46	<b>48.15</b>
	ROUGE-1	15.42	21.59	45.34	53.13	<b>62.82</b>
	ROUGE-L	9.35	14.48	40.80	48.44	<b>58.25</b>
	METEOR	20.33	27.51	33.50	47.32	<b>55.95</b>
	BERTScore	25.99	29.77	50.18	57.81	<b>66.58</b>
Heart	BLEU-1	4.38	5.93	36.44	62.19	<b>69.62</b>
	ROUGE-1	14.45	17.25	70.94	77.15	<b>81.33</b>
	ROUGE-L	5.86	7.64	63.38	69.77	<b>74.35</b>
	METEOR	13.06	15.89	60.25	65.14	<b>72.63</b>
	BERTScore	29.97	31.26	71.59	77.63	<b>79.94</b>
Kidney	BLEU-1	6.29	8.23	70.81	67.37	<b>77.56</b>
	ROUGE-1	16.81	19.54	79.33	76.87	<b>83.42</b>
	ROUGE-L	8.66	10.57	70.77	67.23	<b>74.86</b>
	METEOR	19.12	20.95	72.90	69.71	<b>80.90</b>
	BERTScore	29.14	29.88	83.47	81.46	<b>87.03</b>
Liver	BLEU-1	7.84	10.28	65.51	63.23	<b>74.23</b>
	ROUGE-1	20.12	23.97	73.10	73.63	<b>79.87</b>
	ROUGE-L	10.44	12.69	68.33	66.49	<b>75.06</b>
	METEOR	22.58	24.15	68.97	68.75	<b>78.49</b>
	BERTScore	32.70	32.93	77.00	76.14	<b>82.85</b>
Vessel	BLEU-1	3.45	5.07	50.17	<b>59.56</b>	36.27
	ROUGE-1	11.04	13.45	60.20	<b>70.69</b>	47.63
	ROUGE-L	5.25	7.30	58.35	<b>69.54</b>	44.08
	METEOR	11.62	13.14	55.62	<b>64.98</b>	40.74
	BERTScore	24.09	26.58	67.45	<b>76.82</b>	53.86
Thyroid	BLEU-1	5.86	9.53	49.64	51.86	<b>62.49</b>
	ROUGE-1	15.42	21.28	61.05	65.01	<b>71.74</b>
	ROUGE-L	8.85	13.69	55.44	59.56	<b>67.46</b>
	METEOR	17.23	24.58	58.10	61.06	<b>70.03</b>
	BERTScore	28.71	32.25	66.02	69.69	<b>76.11</b>
Average	BLEU-1	5.94	8.49	55.28	58.70	<b>62.81</b>
	ROUGE-1	15.60	19.57	66.38	70.52	<b>72.51</b>
	ROUGE-L	8.40	11.41	60.51	64.52	<b>67.16</b>
	METEOR	17.42	21.05	60.25	64.05	<b>67.68</b>
	BERTScore	28.51	30.58	70.21	73.99	<b>75.44</b>

Table 3: Comparison results on Ultrasound diagnosis.

Anatomical	Metric↑	LLaVA-OneVision (7B)	Qwen2-VL (7B)	LLaVA-OneVision-Ultrasound (7B)	Qwen2-VL-Ultrasound (7B)	EchoVLM
Breast	BLEU-1	14.28	19.97	<b>31.55</b>	27.67	29.12
	ROUGE-1	31.43	34.15	37.44	37.02	<b>38.07</b>
	ROUGE-L	15.52	20.03	27.62	27.63	<b>28.23</b>
	METEOR	25.73	23.65	<b>26.66</b>	23.26	24.41
	BERTScore	45.74	46.09	<b>49.97</b>	48.42	49.31
Gynecology	BLEU-1	15.05	20.77	<b>29.44</b>	26.36	22.10
	ROUGE-1	31.56	34.40	38.22	38.51	<b>39.17</b>
	ROUGE-L	16.42	21.36	28.61	29.12	<b>29.59</b>
	METEOR	<b>26.61</b>	23.36	26.36	23.98	22.81
	BERTScore	45.79	46.93	50.02	49.63	<b>50.66</b>
Heart	BLEU-1	13.98	18.05	<b>29.68</b>	21.67	22.02
	ROUGE-1	29.15	31.91	34.51	34.30	<b>35.17</b>
	ROUGE-L	15.34	20.12	<b>26.06</b>	25.38	26.05
	METEOR	24.83	21.16	<b>26.11</b>	20.95	21.86
	BERTScore	43.63	44.06	<b>46.59</b>	45.59	46.56
Kidney	BLEU-1	14.93	21.42	<b>28.30</b>	26.45	28.28
	ROUGE-1	32.01	35.37	38.00	38.19	<b>38.76</b>
	ROUGE-L	16.46	22.13	28.25	28.47	<b>29.13</b>
	METEOR	<b>26.64</b>	24.26	25.52	24.14	25.34
	BERTScore	46.80	47.76	49.97	49.79	<b>50.23</b>
Liver	BLEU-1	15.09	22.19	33.43	29.13	<b>33.97</b>
	ROUGE-1	32.33	35.00	38.48	38.45	<b>41.16</b>
	ROUGE-L	16.23	21.57	27.89	28.14	<b>30.32</b>
	METEOR	26.69	23.72	<b>28.58</b>	24.28	28.10
	BERTScore	46.93	47.70	51.03	49.92	<b>52.51</b>
Vessel	BLEU-1	14.34	21.48	<b>31.08</b>	24.57	25.88
	ROUGE-1	32.29	35.50	36.38	36.56	<b>37.69</b>
	ROUGE-L	15.73	21.38	27.70	27.19	<b>27.75</b>
	METEOR	<b>26.87</b>	25.71	26.68	22.41	24.12
	BERTScore	47.68	48.20	49.46	48.62	<b>49.50</b>
Thyroid	BLEU-1	12.77	19.08	<b>30.49</b>	25.96	24.29
	ROUGE-1	27.65	31.68	36.66	<b>37.26</b>	36.95
	ROUGE-L	14.10	19.84	28.15	<b>28.54</b>	28.20
	METEOR	22.92	21.79	<b>26.46</b>	23.14	22.65
	BERTScore	28.71	32.25	<b>66.02</b>	<b>69.69</b>	49.09
Average	BLEU-1	14.35	20.39	<b>30.57</b>	25.97	26.52
	ROUGE-1	30.92	34.00	37.10	37.18	<b>38.14</b>
	ROUGE-L	15.69	20.92	27.75	27.78	<b>28.47</b>
	METEOR	25.76	23.38	<b>26.62</b>	23.17	24.18
	BERTScore	43.61	44.71	<b>51.87</b>	51.67	49.69

Table 4: Comparison results on VQA.

In these equations,  $g_i$  quantifies the contribution of expert  $E_i$ ,  $f_i$  denotes the routing logits, and  $\alpha$  is a learnable scalar that modulates the equilibrium between generic knowledge and ultrasound-specific information.

## Training Strategy

**Stage I: Parameter-isolated pre-training.** All original parameters of the Qwen2-VL are completely frozen, and only the newly-introduced MoE blocks are activated. This isolation strategy prevents catastrophic forgetting of generic multimodal knowledge, steering the expert layers to exclu-

sively acquire domain-specific ultrasound representations.

**Stage II: Cooperative instruction fine-tuning.** We introduce a collaborative optimization mechanism by applying low-rank adaptation (LoRA:  $\mathbf{W} = \mathbf{W}_0 + \Delta\mathbf{W}$ , where  $\Delta\mathbf{W} = \mathbf{A}\mathbf{B}^\top$  with  $\mathbf{A} \in \mathbb{R}^{d \times r}$ ,  $\mathbf{B} \in \mathbb{R}^{d \times r}$ ) (Hu et al. 2021) for lightweight parameter tuning of the base model, while maintaining full parameter updates for the MoE components. Notably, for the architecture comprising frozen FFN layers and activated MoE modules, we develop dynamic modulation parameters  $\lambda \in [0, 1]$  to balance the contributions between general world knowledge and ultrasound domain knowledge.

**Training Objectives.** We optimize the model by minimizing a compound loss that balances the auto-regressive loss with an expert-load-balancing penalty. The vision encoder processes input images to generate  $m$  visual tokens  $V$ . For textual inputs, raw text undergoes tokenization and is subsequently mapped to dense embeddings using an embedding layer, yielding  $n$  textual tokens  $T$ . Their concatenation forms the model input  $X = [V, T]$  of length  $K = m + n$ . During training, the model autoregressively generates a response of length  $L$ ; the autoregressive loss is thus defined as:

$$\mathcal{L}_{\text{ar}} = - \sum_{i=1}^L \log p_{\theta}(y_i | X, y_{<i}) \quad (5)$$

where  $\theta$  is a trainable parameter. To ensure balanced utilization of the  $E$  experts, we introduce an auxiliary load-balancing loss. Let  $g_e(t) \in [0, 1]$  denote the gating weight for expert  $e$  and token  $t$ , where  $\sum_{e=1}^E g_e(t) = 1$ . For a mini-batch of tokens  $\mathcal{B}$ , we compute the dispatch ratio  $F_e$ , representing the fraction of tokens routed to expert  $e$ :

$$F_e = \frac{1}{|\mathcal{B}|} \sum_{t \in \mathcal{B}} \mathbb{I}[g(t) \rightarrow e] \quad (6)$$

where  $g(t) \rightarrow e$  denotes that token  $t$  is routed to expert  $e$ ,  $\mathbb{I}[\cdot]$  is the indicator function that equals 1 if token  $t$  is routed to expert  $e$ , and 0 otherwise. The average gating probability is defined as:

$$G_e = \frac{1}{|\mathcal{B}|} \sum_{t \in \mathcal{B}} g_e(t). \quad (7)$$

The auxiliary balancing loss is then given by:

$$\mathcal{L}_{\text{bal}} = \sum_{e=1}^E F_e G_e. \quad (8)$$

The overall training objective combines both components:

$$\mathcal{L}_{\text{total}} = \mathcal{L}_{\text{ar}} + \gamma \mathcal{L}_{\text{bal}} \quad (9)$$

where  $\gamma$  is a hyperparameter controlling the strength of the load-balancing penalty.

## Experiments

### Implementation Details

As presented in Table 1, the two-stage training framework utilizes distinct datasets tailored to each phase. In Stage I, we

initialize the newly introduced MoE modules using a dataset comprising 208,941 processed clinical reports and 1.47 million ultrasound key frames. This phase focuses exclusively on enabling the MoE components to capture domain-specific visual and textual patterns, without altering the pre-trained parameters of the base model.

Subsequently, Stage II implements Cooperative Instruction Fine-tuning, during which the model is trained on 1.8 million instruction-following samples. This stage aims to enhance the model’s ability to understand and respond to diverse user instructions while integrating both the base model and the MoE modules in a collaborative manner. The training procedure follows the protocol established by LLaVA-Med, and further implementation details, including optimization settings and hyperparameter configurations, are provided in the Supplementary Material.

To ensure reproducible empirical results, we evaluate the trained model on the held-out test set, which comprises 27 577 ultrasound images and 3 000 corresponding reports. During inference, all responses are generated with greedy decoding; no sampling stochasticity is introduced, guaranteeing deterministic outputs across runs.

## Results

**Report Generation.** Table 2 shows EchoVLM consistently outperforms general (LLaVA-OneVision, Qwen2-VL) and ultrasound-specialized models (LLaVA-OneVision-Ultrasound, Qwen2-VL-Ultrasound) across six anatomical domains (breast, gynecology, heart, kidney, liver, thyroid), achieving state-of-the-art BERTScores (e.g., heart: 89.80; kidney: 75.89). However, the model exhibits suboptimal results in vascular analysis. We hypothesize that this stems from the long-tailed distribution of the overall dataset, with vascular cases forming the smallest proportion. This scarcity likely led domain experts to prioritize dominant anatomical patterns from majority classes (e.g., breast/liver) during annotation, inadvertently marginalizing subtle vascular features. Collectively, these results demonstrate EchoVLM’s robustness for prevalent structures while underscoring that vascular performance could benefit from data rebalancing strategies.

**Ultrasound Diagnosis.** Ultrasound diagnosis represents a concise yet highly specialized synthesis of the comprehensive sonographic examination findings, requiring precise integration of anatomical observations and pathological interpretations into clinical reports. To validate EchoVLM’s capability in automating this critical task, we systematically evaluate its performance against established baselines across seven anatomical domains. The results in Table 3 demonstrate that EchoVLM outperforms baseline models in most anatomical categories, achieving state-of-the-art results on kidney (BLEU-1: 77.56, BERTScore: 87.03), liver (ROUGE-1: 79.87, BERTScore: 82.85), which reflects its strong semantic alignment with clinical terminology and superior diagnostic reasoning capacity.

**Vision Question Answering.** Ultrasound VQA typically demands models with hierarchical comprehension capabilities to satisfy heterogeneous clinical requirements. Such

Task	Metric↑	w/o Share Expert	w Share Expert
Report Generation	BLEU-1	49.29	53.87 (+4.58)
	ROUGE-1	58.42	61.69 (+3.27)
	ROUGE-L	52.33	55.78 (+3.45)
	METEOR	49.54	53.16 (+3.62)
	BERTScore	70.11	71.38 (+1.27)
Ultrasound Diagnosis	BLEU-1	59.33	62.81 (+3.48)
	ROUGE-1	67.46	72.51 (+5.05)
	ROUGE-L	61.67	67.16 (+5.49)
	METEOR	64.92	67.67 (+2.75)
	BERTScore	71.38	75.43 (+4.05)
VQA	BLEU-1	31.15	26.52 (-4.63)
	ROUGE-1	35.92	38.14 (+2.22)
	ROUGE-L	27.25	28.47 (+1.22)
	METEOR	26.41	24.18 (-2.23)
	BERTScore	48.77	49.69 (+0.92)

Table 5: Ablation study of the shared expert.

Task(4 Experts)	Metric↑	Top1	Top2
Report Generation	BLEU-1	49.93	53.87 (+3.94)
	ROUGE-1	58.80	61.69 (+2.89)
	ROUGE-L	52.97	55.78 (+2.81)
	METEOR	49.87	53.16 (+3.29)
	BERTScore	70.54	71.38 (+0.84)
Ultrasound Diagnosis	BLEU-1	58.71	62.81 (+4.1)
	ROUGE-1	67.75	72.51 (+4.76)
	ROUGE-L	62.16	67.16 (+5.00)
	METEOR	64.73	67.67 (+2.94)
	BERTScore	72.20	75.43 (+3.23)
VQA	BLEU-1	31.11	26.52 (-4.59)
	ROUGE-1	35.79	38.14 (+2.35)
	ROUGE-L	27.04	28.47 (+1.43)
	METEOR	26.73	24.18 (-2.55)
	BERTScore	48.75	49.69 (+0.94)

Table 6: Ablation study of Top-K routing strategies.

multi-level proficiency is imperative for decision support for both radiologists and referring physicians. Hence, comparative experiments were conducted and reported in Table 4. Collectively, EchoVLM exhibits a balanced performance, surpassing the baselines in 16 of 35 metric-anatomy combinations and ranking second in an additional 10. Notably, these results demonstrate the effectiveness of leveraging a MoE (Mixture of Experts) architecture in achieving effective knowledge transfer to domain-specific ultrasound tasks. However, improving answer accuracy remains a pivotal avenue for future research.

### Ablation Study

**Impact of the share expert.** The ablation study in Table 5 demonstrates that integrating shared experts into the MoE framework improves performance for medical report generation and ultrasound diagnosis, with BLEU-1 gains of +4.58 and +3.48, ROUGE-L increases of +3.45 and +5.49, and BERTScore improvements of +1.27 and +4.05, respectively. These results indicate that shared experts enhance cross-task knowledge transfer and multimodal coherence in tasks re-

Task	Metric↑	0 Expert	2 Experts	4 Experts
Report Generation	BLEU-1	43.72	50.33	<b>53.87</b>
	ROUGE-1	56.92	58.75	<b>61.69</b>
	ROUGE-L	49.77	52.74	<b>55.78</b>
	METEOR	44.76	50.33	<b>53.16</b>
Ultrasound Diagnosis	BERTScore	70.17	70.51	<b>71.38</b>
	BLEU-1	58.70	59.66	<b>62.81</b>
	ROUGE-1	70.52	68.02	<b>72.51</b>
	ROUGE-L	64.52	62.45	<b>67.16</b>
VQA	METEOR	64.05	65.59	<b>67.67</b>
	BERTScore	73.99	72.16	<b>75.43</b>
	BLEU-1	25.97	<b>31.19</b>	26.52
	ROUGE-1	37.18	35.93	<b>38.14</b>
VQA	ROUGE-L	27.78	27.21	<b>28.47</b>
	METEOR	23.17	<b>26.60</b>	24.18
	BERTScore	48.72	48.89	<b>49.69</b>

Table 7: Ablation study of expert numbers

quiring complex semantic synthesis.

**Impact of the Top-K Routing.** To investigate the impact of expert activation mechanisms within the Mixture of Experts (MoE) architecture, we implement two widely adopted routing strategies: Top-1 and Top-2 activation. As shown in Table 6, ablation studies demonstrate that Top-2 routing generally achieves superior performance in complex multimodal tasks compared to Top-1 routing, although the magnitude of improvement varies across task characteristics. For report generation tasks, Top-2 routing enhances all evaluation metrics (e.g., +3.94 absolute improvement in BLEU-1 for report generation), while ultrasound diagnostic tasks exhibit significant gains in ROUGE-L (+5.00 absolute improvement). These results indicate that activating two specialized experts facilitates more effective knowledge integration and contextual understanding.

**Impact of the Number of Experts.** The number of experts represents a critical hyperparameter in EchoVLM, where prior studies have demonstrated that scaling this parameter yields performance benefits. However, its applicability within the ultrasound domain remains underexplored, necessitating systematic investigation through ablation studies. To address this gap, we conducted an ablation experiment expanding the expert count from 0 to 4, specifically to determine whether the capacity gains observed in general vision-language models could be effectively transferred to ultrasound-specific tasks characterized by distinct modality interactions and diagnostic complexity. Our findings demonstrate statistically significant improvements in high-complexity tasks, including report generation (+10.15 BLEU-1) and ultrasound diagnosis (+4.11 BLEU-1), indicating that increased model capacity enhances fine-grained cross-modal alignment and representation learning. These results suggest that the intricate spatial-temporal patterns in ultrasound imaging and the nuanced semantic dependencies in medical reporting benefit substantially from specialized expert subnetworks.

## Conclusion

In this study, we introduced EchoVLM, the first ten-billion-parameter universal ultrasound-specialized VLM. Our work establishes three pivotal contributions: (1) the curation of the largest multi-organ ultrasound dataset comprising 208,941 clinical cases and 1.47 million images spanning seven anatomical regions; (2) the development of a novel few-shot prompting mechanism with expert validation that constructs a robust multi-task instruction-tuning pipeline for ultrasound diagnostics; and (3) the integration of a Dual-path MoE architecture with dynamic routing that significantly enhances model adaptability to ultrasound's heterogeneous imaging characteristics. Experimental validation demonstrated EchoVLM's superior performance over Qwen2-VL and LLaVA-OneVision across multiple anatomical domains. Despite these advances, limitations persist in dataset long-tail distribution and complex visual question answering requiring multi-step reasoning. Future work will address data rebalancing, expanded anatomical coverage, longitudinal patient integration, and refined routing to advance precise, efficient AI-assisted ultrasound diagnostics.

## References

- Alayrac, J.-B.; Donahue, J.; Luc, P.; Miech, A.; Barr, I.; Hasson, Y.; Lenc, K.; Mensch, A.; Millicah, K.; Reynolds, M.; Ring, R.; Rutherford, E.; Cabi, S.; Han, T.; Gong, Z.; Samangoeei, S.; Monteiro, M.; Menick, J.; Borgeaud, S.; Brock, A.; Nematzadeh, A.; Sharifzadeh, S.; Binkowski, M.; Barreira, R.; Vinyals, O.; Zisserman, A.; and Simonyan, K. 2022. Flamingo: a visual language model for few-shot learning. In *Proceedings of the 36th International Conference on Neural Information Processing Systems, NIPS '22*. Red Hook, NY, USA: Curran Associates Inc. ISBN 9781713871088.
- Bai, J.; Bai, S.; Yang, S.; Wang, S.; Tan, S.; Wang, P.; Lin, J.; Zhou, C.; and Zhou, J. 2023. Qwen-VL: A Versatile Vision-Language Model for Understanding, Localization, Text Reading, and Beyond. arXiv:2308.12966.
- Chen, H.; Lin, J.; Chen, X.; Fan, Y.; Jin, X.; Su, H.; Dong, J.; Fu, J.; and Shen, X. 2025. Rethinking Visual Layer Selection in Multimodal LLMs. arXiv:2504.21447.
- Fan, X.; Ji, T.; Jiang, C.; Li, S.; Jin, S.; Song, S.; Wang, J.; Hong, B.; Chen, L.; Zheng, G.; Zhang, M.; Huang, C.; Zheng, R.; Xi, Z.; Zhou, Y.; Dou, S.; Ye, J.; Yan, H.; Gui, T.; Zhang, Q.; Qiu, X.; Huang, X.; Wu, Z.; and Jiang, Y.-G. 2024. MouSi: Poly-Visual-Expert Vision-Language Models. arXiv:2401.17221.
- Guo, Q.; Mello, S. D.; Yin, H.; Byeon, W.; Cheung, K. C.; Yu, Y.; Luo, P.; and Liu, S. 2024. RegionGPT: Towards Region Understanding Vision Language Model. arXiv:2403.02330.
- Hong, W.; Wang, W.; Ding, M.; Yu, W.; Lv, Q.; Wang, Y.; Cheng, Y.; Huang, S.; Ji, J.; Xue, Z.; Zhao, L.; Yang, Z.; Gu, X.; Zhang, X.; Feng, G.; Yin, D.; Wang, Z.; Qi, J.; Song, X.; Zhang, P.; Liu, D.; Xu, B.; Li, J.; Dong, Y.; and Tang, J. 2024. CogVLM2: Visual Language Models for Image and Video Understanding. arXiv:2408.16500.
- Hu, E. J.; Shen, Y.; Wallis, P.; Allen-Zhu, Z.; Li, Y.; Wang, S.; Wang, L.; and Chen, W. 2021. LoRA: Low-Rank Adaptation of Large Language Models. arXiv:2106.09685.
- Kar, O. F.; Tonioni, A.; Poklukar, P.; Kulshrestha, A.; Zamir, A.; and Tombari, F. 2024. BRAVE: Broadening the visual encoding of vision-language models. arXiv:2404.07204.
- Li, B.; Zhang, Y.; Guo, D.; Zhang, R.; Li, F.; Zhang, H.; Zhang, K.; Zhang, P.; Li, Y.; Liu, Z.; and Li, C. 2024. LLaVA-OneVision: Easy Visual Task Transfer. arXiv:2408.03326.
- Li, C.; Wong, C.; Zhang, S.; Usuyama, N.; Liu, H.; Yang, J.; Naumann, T.; Poon, H.; and Gao, J. 2023a. LLaVA-Med: Training a Large Language-and-Vision Assistant for Biomedicine in One Day. arXiv:2306.00890.
- Li, J.; Li, D.; Savarese, S.; and Hoi, S. 2023b. BLIP-2: bootstrapping language-image pre-training with frozen image encoders and large language models. In *Proceedings of the 40th International Conference on Machine Learning, ICML'23*. JMLR.org.
- Li, X.; Zheng, Y.; Chen, H.; Chen, X.; Liang, Y.; Lai, C.; Li, B.; and Xue, X. 2026. Instruction-guided fusion of multi-layer visual features in Large Vision-Language Models. *Pattern Recognition*, 170: 111932.
- Lin, B.; Ye, Y.; Zhu, B.; Cui, J.; Ning, M.; Jin, P.; and Yuan, L. 2024a. Video-LLaVA: Learning United Visual Representation by Alignment Before Projection. In Al-Onaizan, Y.; Bansal, M.; and Chen, Y.-N., eds., *Proceedings of the 2024 Conference on Empirical Methods in Natural Language Processing*, 5971–5984. Miami, Florida, USA: Association for Computational Linguistics.
- Lin, J.; Yin, H.; Ping, W.; Molchanov, P.; Shoeybi, M.; and Han, S. 2024b. VILA: On Pre-training for Visual Language Models. In *2024 IEEE/CVF Conference on Computer Vision and Pattern Recognition (CVPR)*, 26679–26689. Los Alamitos, CA, USA: IEEE Computer Society.
- Liu, F.; Lin, K.; Li, L.; Wang, J.; Yacoob, Y.; and Wang, L. 2024a. Mitigating Hallucination in Large Multi-Modal Models via Robust Instruction Tuning. In *The Twelfth International Conference on Learning Representations*.
- Liu, H.; Li, C.; Li, Y.; and Lee, Y. J. 2024b. Improved Baselines with Visual Instruction Tuning. In *2024 IEEE/CVF Conference on Computer Vision and Pattern Recognition (CVPR)*, 26286–26296. Los Alamitos, CA, USA: IEEE Computer Society.
- Liu, H.; Li, C.; Wu, Q.; and Lee, Y. J. 2023. Visual Instruction Tuning. In Oh, A.; Naumann, T.; Globerson, A.; Saenko, K.; Hardt, M.; and Levine, S., eds., *Advances in Neural Information Processing Systems*, volume 36, 34892–34916. Curran Associates, Inc.
- Radford, A.; Kim, J. W.; Hallacy, C.; Ramesh, A.; Goh, G.; Agarwal, S.; Sastry, G.; Askell, A.; Mishkin, P.; Clark, J.; Krueger, G.; and Sutskever, I. 2021. Learning Transferable Visual Models From Natural Language Supervision. arXiv:2103.00020.
- Tong, S.; Liu, Z.; Zhai, Y.; Ma, Y.; LeCun, Y.; and Xie, S. 2024. Eyes Wide Shut? Exploring the Visual Shortcomings

of Multimodal LLMs . In *2024 IEEE/CVF Conference on Computer Vision and Pattern Recognition (CVPR)*, 9568–9578. Los Alamitos, CA, USA: IEEE Computer Society.

Vasu, P. K. A.; Pouransari, H.; Faghri, F.; Vemulapalli, R.; and Tuzel, O. 2024. MobileCLIP: Fast Image-Text Models through Multi-Modal Reinforced Training . In *2024 IEEE/CVF Conference on Computer Vision and Pattern Recognition (CVPR)*, 15963–15974. Los Alamitos, CA, USA: IEEE Computer Society.

Wang, W.; Lv, Q.; Yu, W.; Hong, W.; Qi, J.; Wang, Y.; Ji, J.; Yang, Z.; Zhao, L.; Song, X.; Xu, J.; Chen, K.; Xu, B.; Li, J.; Dong, Y.; Ding, M.; and Tang, J. 2024. CogVLM: Visual Expert for Pretrained Language Models. In Globerson, A.; Mackey, L.; Belgrave, D.; Fan, A.; Paquet, U.; Tomczak, J.; and Zhang, C., eds., *Advances in Neural Information Processing Systems*, volume 37, 121475–121499. Curran Associates, Inc.

Wang, Y.; Kordi, Y.; Mishra, S.; Liu, A.; Smith, N. A.; Khashabi, D.; and Hajishirzi, H. 2023. Self-Instruct: Aligning Language Models with Self-Generated Instructions. arXiv:2212.10560.

Zhang, B.; Zhang, P.; Dong, X.; Zang, Y.; and Wang, J. 2024a. Long-CLIP: Unlocking the Long-Text Capability of CLIP. arXiv:2403.15378.

Zhang, T.; Li, X.; Fei, H.; Yuan, H.; Wu, S.; Ji, S.; Loy, C. C.; and YAN, S. 2024b. OMG-LLaVA: Bridging Image-level, Object-level, Pixel-level Reasoning and Understanding. In *The Thirty-eighth Annual Conference on Neural Information Processing Systems*.

Zhang, Y.; Zhang, R.; Gu, J.; Zhou, Y.; Lipka, N.; Yang, D.; and Sun, T. 2024c. LLaVAR: Enhanced Visual Instruction Tuning for Text-Rich Image Understanding. arXiv:2306.17107.

## Appendix

### Model Architecture and Training Configuration

As presented in Table 8, we detail the model architecture and our proposed two-stage training framework, which integrates a Dual-path MoE for incremental training to enhance domain-specific adaptation. Specifically, the routing experts within this MoE are configured with a dimensionality of 1408 (Bai et al. 2023), adhering to the Qwen model specifications, while employing a Top-2 selection strategy among four experts to balance specialization and efficiency; concurrently, the shared expert dimension is established at four times that of the routing experts to ensure sufficient capacity for acquiring comprehensive general ultrasound knowledge. Additionally, the PatchMerger module facilitates the fusion and compression of visual representations by consolidating adjacent  $2 \times 2$  tokens into a single token, thereby optimizing visual feature processing. During Stage I, the base model parameters are maintained in a frozen state to preserve pre-trained representations, with optimization strictly confined to the newly integrated Dual-path MoE components for acquiring domain-specific visual-textual patterns. In the subsequent Stage II, Cooperative Instruction Fine-tuning is implemented via Low-Rank Adaptation (LoRA), selectively up-

Config	Stage I	Stage II
Image encoder	CLIP-ViT-L/14	
Vision-to-text projection	MLP	
LLM	Qwen2-7B	
PatchMerger rate	4	
Shared expert number	1	
Shared expert dimension	5632	
Routing expert number	4	
Routing expert dimension	1408	
Top-k	2	
Feature select layer	-1	
Image resolution	392×392	
LoRA rank	-	8
LoRA alpha	-	16
LoRA dropout	-	0.05
DeepSpeed	Zero2	
Epoch	1	
Optimizer	AdamW	
Weight decay	0.0	
Learning rate	1e-3	2e-5
Learning rate schedule	Cosine	
Warmup ratio	0.03	
Max length	32768	
Batch size per GPU	1	
GPU	H100-80G, 2×A100-80G	
Gradient checkpointing	True	
Precision	Bf16	
Auxiliary loss weight $\gamma$	0.001	
Training parameters	3.39B	3.4B
Total parameters	11B	

Table 8: Model Architecture and Training Configuration.

dating the visual encoder, vision-to-text projection layer, and large language model attention layers, while concurrently enabling full-parameter updates for the active experts within the Dual-path MoE to maintain their domain-specialized adaptation capabilities.

### Data Generation Pipeline Implementation.

The data generation pipeline integrates rigorous deduplication protocols to ensure content diversity, implementing ROUGE-L and Simhash-based deduplication during instance generation: any newly generated instance is discarded if its ROUGE-L similarity exceeds 0.7 against any prior instance or if its Simhash similarity—quantified by a Hamming distance threshold of  $\leq 3$ —indicates substantial overlap. For the open-ended subset, subsequent to AI pre-screening, 5% of batches (with 10 samples per batch) are randomly selected for clinical validation conducted by domain experts. If errors or inappropriate samples are identified in a selected batch, the generation strategy or model associated with the batch’s source data is subjected to retrospective analysis and adjustment (e.g., model replacement). This targeted revision mechanism facilitates the resolution of potential issues in the generation process, thereby sustaining enhancements to the reliability of the overall dataset.

## Routing Distributions

In this section, we conduct a comprehensive analysis of the routing distribution within the MoE framework to rigorously evaluate its efficacy and load-balancing performance. As illustrated in Figure 5, the aggregate routing frequencies across all experts exhibit a remarkably balanced pattern, demonstrating that no single expert is disproportionately over- or under-utilized. Delving deeper into modality-specific routing behavior, we observe that the overwhelming majority of dispatched tokens correspond to image data, whereas textual tokens constitute a markedly smaller fraction. This pronounced imbalance originates from an inherent bias in our dataset composition: although we possess 208,941 radiological reports, these are accompanied by 1.47 million key-frame ultrasound images. Consequently, each individual report is associated with multiple images, thereby skewing the token distribution toward visual content and explaining the dominant image-centric routing observed across experts.

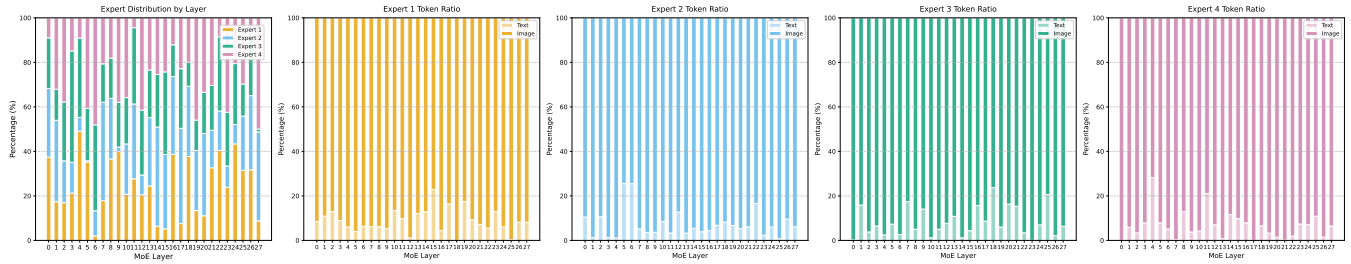
## Visualization

To elucidate the internal decision-making process of VLMs, we employed the Grad-CAM heatmap visualization technique proposed by Zhang et al. (?), where warmer regions (depicted in red) in Figure 6 indicate pixels exhibiting the strongest gradient flow towards the predicted token logit, signifying that the model primarily attends to these semantically significant regions during textual output generation, whereas cooler regions (in blue) receive negligible weight allocation, implying minimal contribution to the prediction; the visualized attention patterns confirm that the VLM’s language reasoning is grounded in semantically relevant visual features such as anatomical landmarks, quantitative measurements, and hemodynamic bar charts—highlighted within red bounding boxes—rather than spurious correlations, yet the model also exhibits attention to non-informative regions including image edges and black areas—highlighted within blue bounding boxes—which lack semantic utility, thereby highlighting a persistent challenge in VLMs: the coexistence of semantic consistency (focusing on task-critical visual elements) and spurious associations (distracting attention to noise or irrelevant artifacts); future work should enhance model robustness and interpretability through strategies such as attention regularization, constrained attention routing, and explicit mitigation of spurious associations.

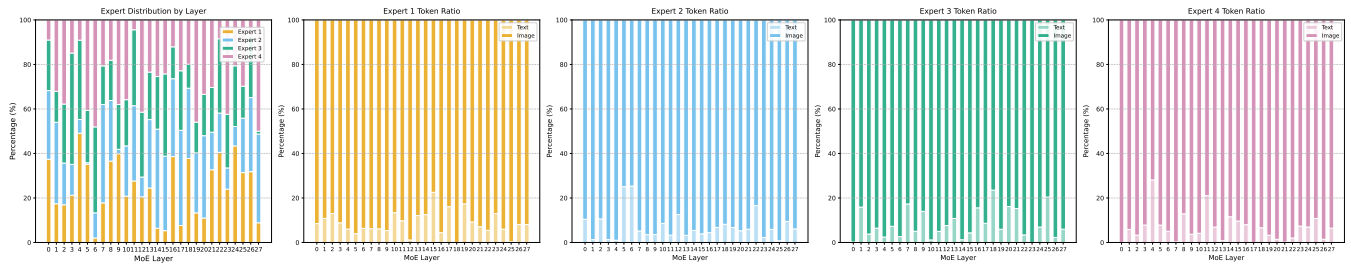
## Case Study

In Figures 7-13, we present an analysis of report generation cases covering different anatomical regions. Due to space limitations, this section randomly selects examples for discussion. This random selection method ensures an objective assessment of the model’s capabilities while maintaining scientific rigor. The results show that our model exhibits significant advantages over both general-purpose and specialized ultrasound models, effectively capturing clinically meaningful information from images to support accurate reasoning and report generation. Despite these advantages,

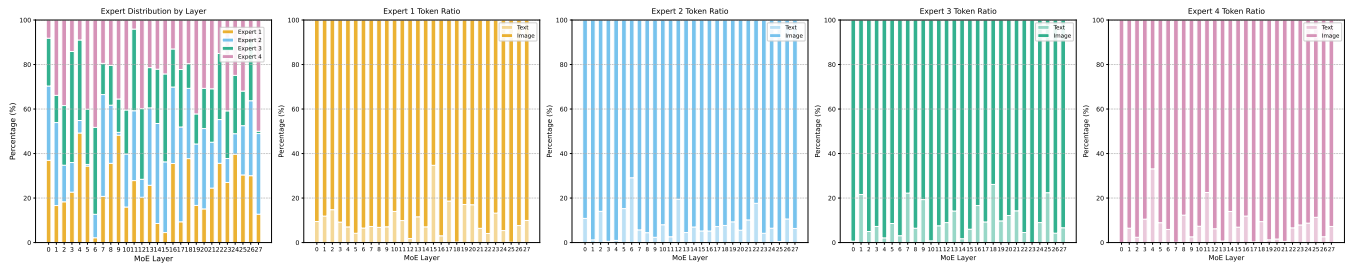
some limitations exist, including false negatives in nodule identification, suggesting that there is still room for improvement.



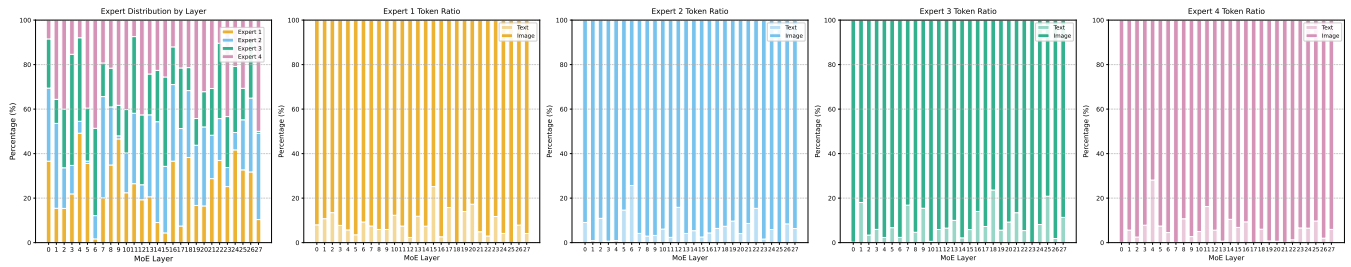
(a) Breast



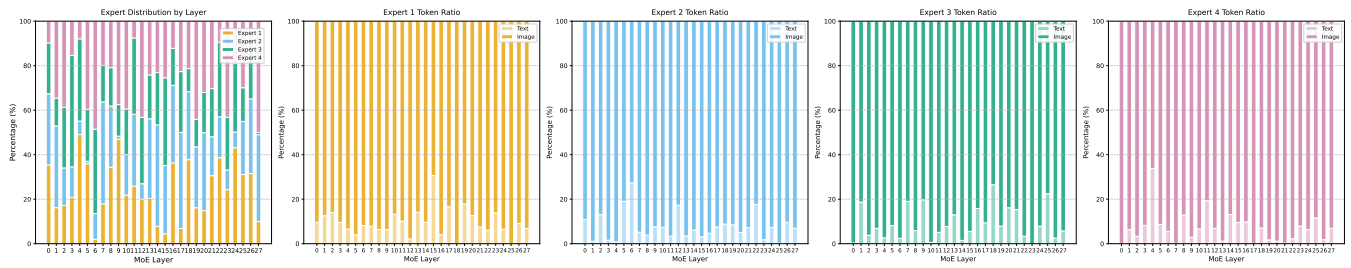
(b) Gynaecology



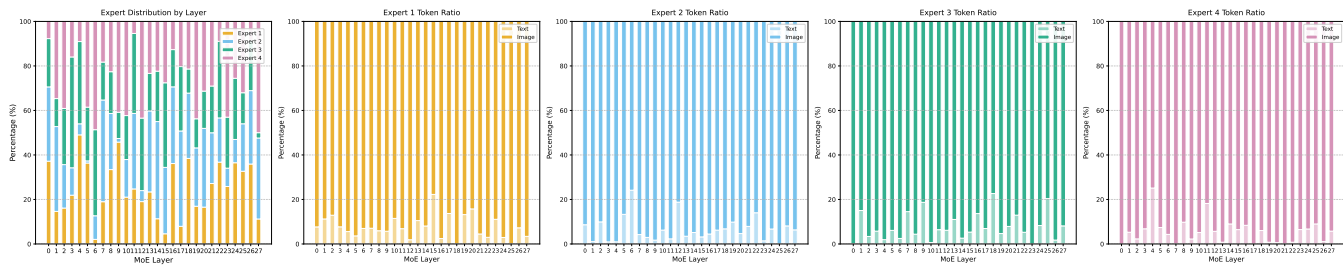
(c) Heart



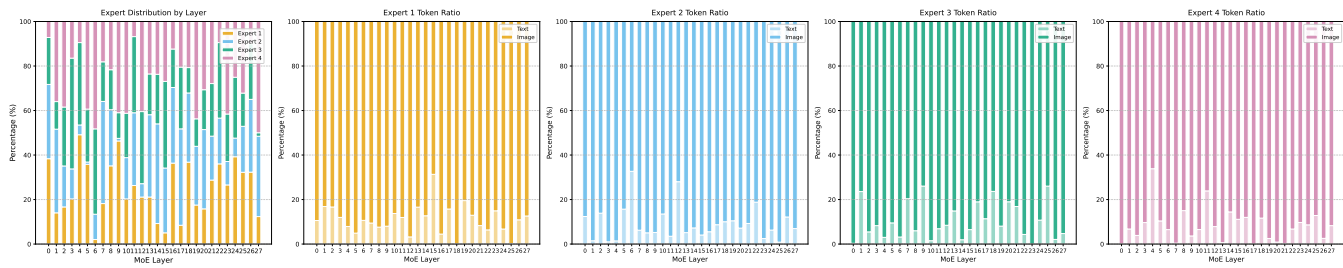
(d) Kidney



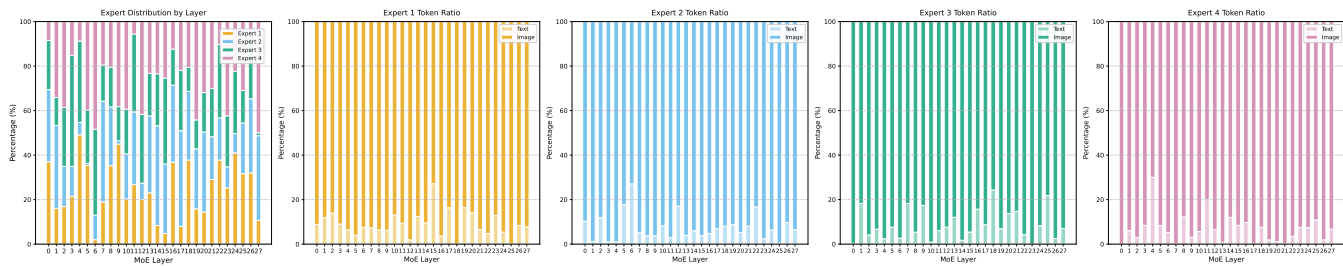
(e) Liver



(f) Thyroid

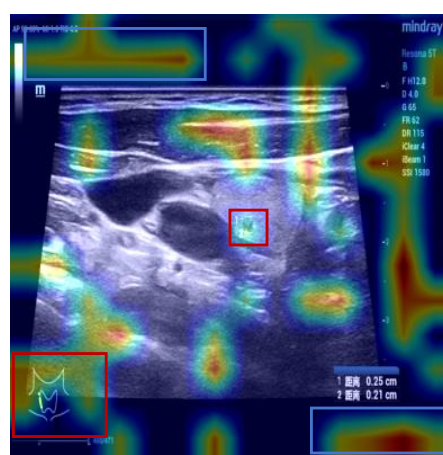
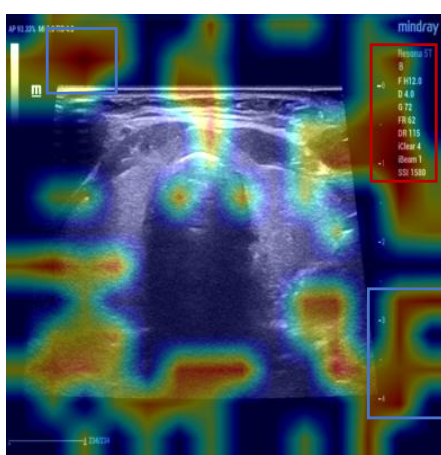
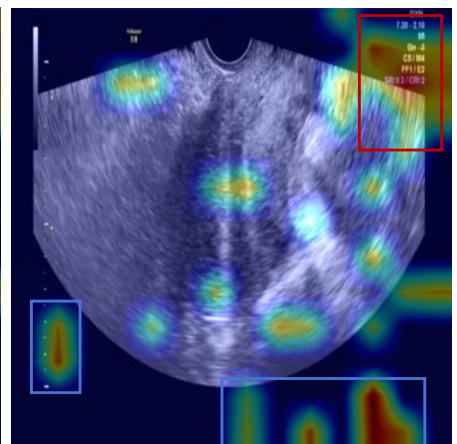
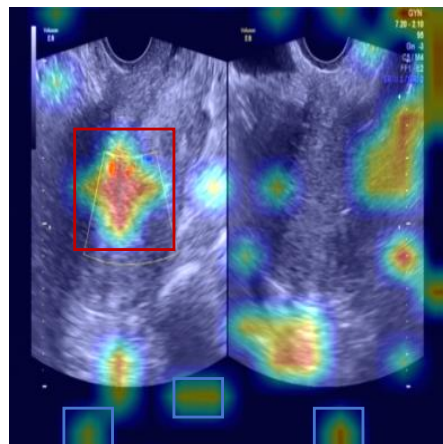
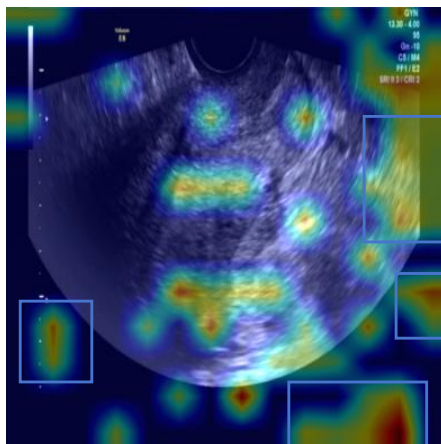
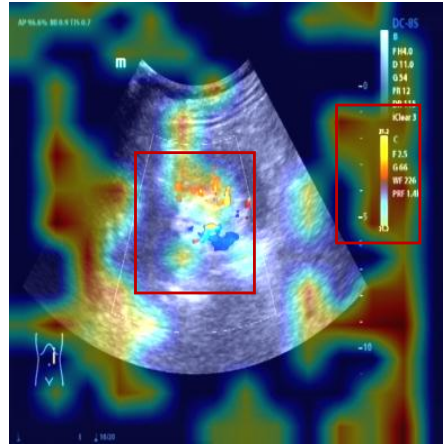
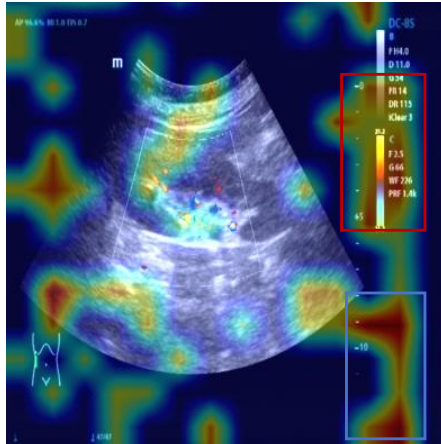
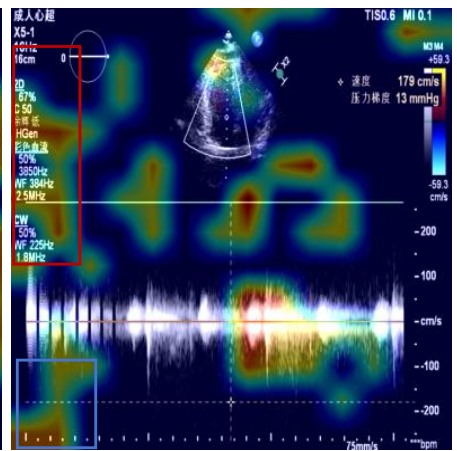
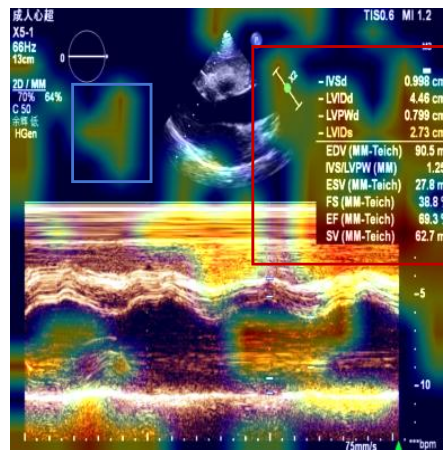
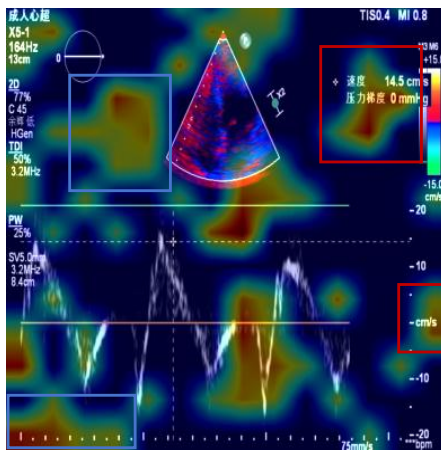


(g) Vessel



(h) Overall

Figure 5: Expert routing distribution analysis for different medical imaging tasks: (a) Breast, (b) Gynaecology, (c) Heart, (d) Kidney, (e) Liver, (f) Thyroid, (g) Vessel, and (h) Overall



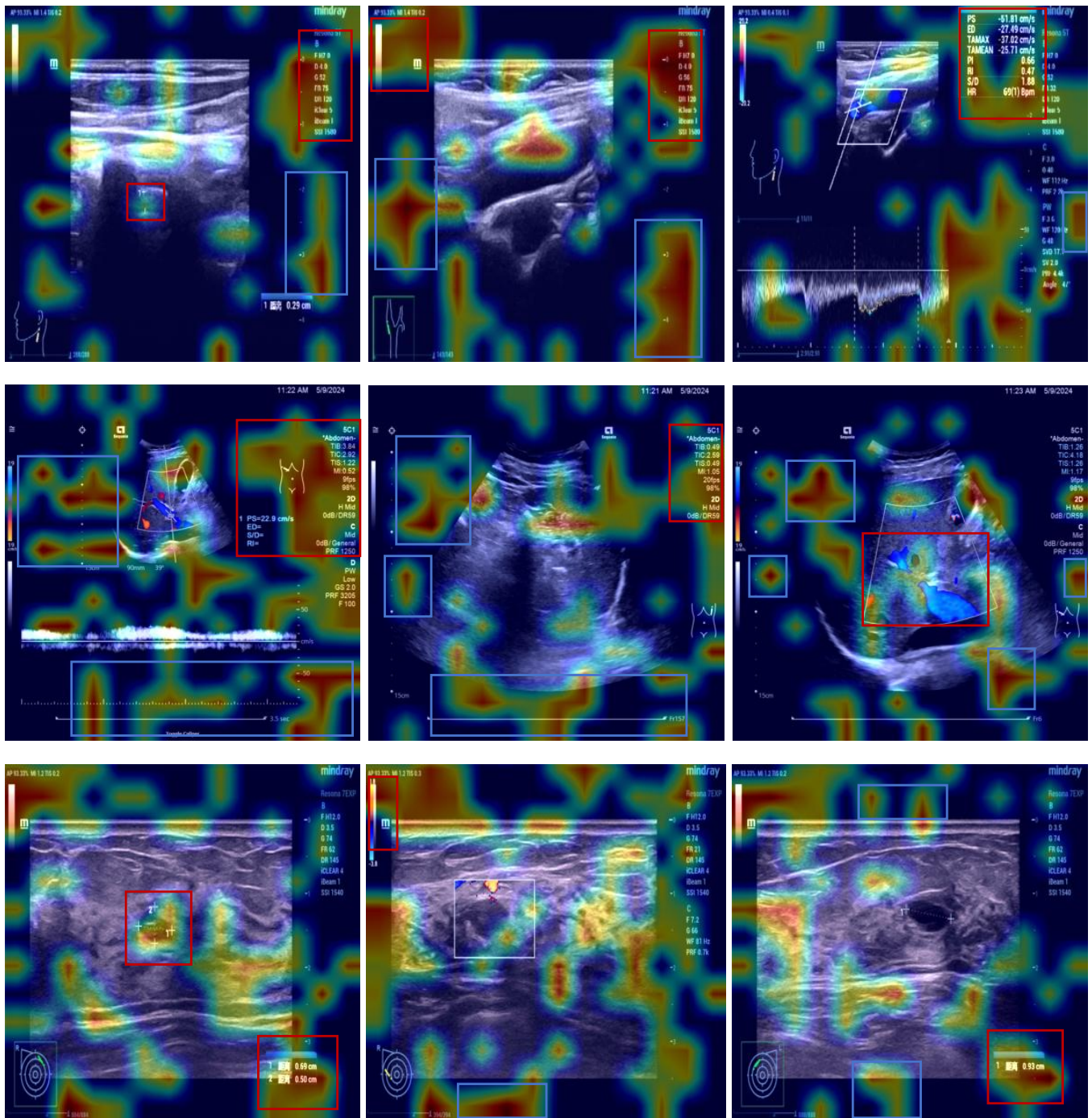
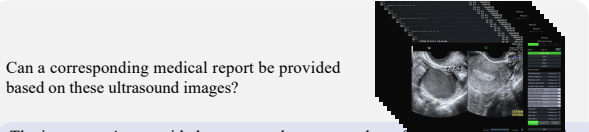


Figure 6: Visualization results. Red boxes highlight meaningful regions, while blue boxes indicate irrelevant or meaningless areas.



Can a corresponding medical report be provided based on these ultrasound images?

LLaVA-OneVision

The image you've provided appears to be a screenshot of a medical ultrasound imaging software interface, showing various ultrasound images and measurements. However, without the actual ultrasound images or a clear view of the specific findings, it's not possible to provide a detailed medical report based on these images alone. A medical report typically includes:

1. Patient information: Name, age, date of birth, etc.
2. Clinical history: Reason for the ultrasound, symptoms, and medical history.
3. Technical details: Type of ultrasound, settings used, and the probe frequency.
4. Description of findings: Detailed observations of the ultrasound images, including any abnormalities or normal findings.
5. Measurements: Quantitative data such as size, shape, and other dimensions of structures observed.
6. Interpretation: Clinical significance of the findings, including any diagnoses or recommendations.
7. Conclusion: Summary of the report and any follow-up recommendations.

To provide a corresponding medical report, a healthcare professional would need to:

- Review the ultrasound images in detail.
- Compare the images to clinical findings and medical history.
- Use their professional judgment to interpret the images and make a diagnosis.
- Write a comprehensive report that includes all the necessary information.

If you have specific questions about the ultrasound images or need an interpretation of the findings, it would be best to consult with a qualified healthcare provider, such as a radiologist or a specialist in the field related to the ultrasound (e.g., obstetrician for obstetric ultrasounds). They can provide a detailed medical report based on their expertise and the context of the patient's care.

Qwen2-VL

Yes, a corresponding medical report can be provided based on these ultrasound images. The images appear to be ultrasound scans of the pelvic region, likely for gynecological purposes. The report would typically include the following information:

1. **\*\*Patient Information\*\***: Name, age, date of the scan, and any relevant medical history.
2. **\*\*Technical Details\*\***: Date and time of the scan, machine settings, and any specific techniques used.
3. **\*\*Findings\*\***: Description of any abnormalities or normal findings in the pelvic organs, such as the uterus, ovaries, and surrounding structures.
4. **\*\*Measurements\*\***: Any measurements taken, such as the size of the uterus or ovaries.
5. **\*\*Impressions\*\***: Interpretation of the findings by the radiologist, including any recommendations for further testing or treatment.
6. **\*\*Signatures\*\***: Signatures of the radiologist and any other relevant healthcare providers.

If you have access to the full report, it would provide a comprehensive overview of the findings and recommendations.

LLaVA-OneVision-Ultrasound

Transvaginal, transabdominal, and color Doppler ultrasound examinations revealed a normal uterine size of 64 mm in length, 41 mm in anteroposterior diameter, and 48 mm in transverse diameter. The endometrium was 11 mm thick and had a homogeneous echogenicity. The myometrium was also homogeneous in echogenicity. The ovaries were clear bilaterally, and no abnormal masses were found in the adnexal areas. Pelvic color Doppler ultrasound revealed no abnormal blood flow signals.

Qwen2-VL-Ultrasound

Transvaginal, transabdominal, and color Doppler ultrasound examinations revealed a normal uterine size of 54 mm in length, 40 mm in anteroposterior diameter, and 49 mm in transverse diameter. The endometrium was 10 mm thick and had a homogeneous echogenicity. The myometrium was also homogeneous in echogenicity. The left ovary was well-defined. No abnormal mass was observed in the left adnexal region. A 24 mm × 21 mm anechoic area was observed in the right ovary, with a well-defined, oval shape. No color flow signal was observed in the cyst wall.

EchoVLM

Transvaginal, transabdominal, and color Doppler ultrasound examinations revealed a normal uterine size of 64 mm in length, 46 mm in anteroposterior diameter, and 57 mm in transverse diameter. The endometrium was 10 mm thick and had a homogeneous echogenicity. The myometrium was also homogeneous in echogenicity. The ovaries were clear bilaterally, and no abnormal masses were found in the adnexal areas. Pelvic color Doppler ultrasound revealed no abnormal blood flow signals.

Ground truth

The uterus was enlarged, measuring 64 mm in length, 46 mm in anteroposterior diameter, and 57 mm in transverse diameter. The endometrium was 9 mm thick and had uneven echogenicity. The myometrium was heterogeneous in echogenicity. A hypoechoic area measuring 9 mm × 8 mm was observed on the left wall. Hypoechoic areas measuring 16 mm × 11 mm and 14 mm × 11 mm were observed on the right anterior wall, with small streaks of color flow signal within the lesion. The cervical canal was present. The left ovary was clear. No abnormal mass was observed in the left adnexal region. A 44 mm × 33 mm, well-defined, oval mass with a cloudy echogenicity was observed on the right ovary. No color flow signal was observed in the cystic wall.

Figure 7: Gynecological Case Study.

根据这些超声图像能否提供相应的医疗报告？



这张图片是一张医学超声成像图像，具体来说是腹部超声图像。图像显示了人体内部的器官和组织，通过不同颜色的声波反射来区分不同的结构。图像中可以看到多种颜色，包括蓝色、红色和彩色混合，这些颜色代表了血液的流动方向和速度。蓝色通常表示血液流向探头，而红色表示血液远离探头，彩色混合则表示血液在两个方向流动。

在图像的左上角，有一个垂直的彩色条，显示了速度范围 (0.0-10.0 cm/s) 和深度范围 (0.0-15.0 cm)，以及一个比例尺 (Scale 18 cm)。在图像的右上角，有一个类似的垂直彩色条，显示了速度范围 (0.0-10.0 cm/s) 和深度范围 (0.0-15.0 cm)，以及一个比例尺 (Scale 18 cm)。这些条帮助医生理解图像中不同颜色的声波反射所代表的血液流动情况。

在图像的底部，有一个水平的彩色条，显示了速度范围 (0.0-10.0 cm/s) 和深度范围 (0.0-15.0 cm)，以及一个比例尺 (Scale 18 cm)。这个条帮助医生理解图像中不同颜色的声波反射所代表的血液流动情况。

图像的左下角有一个小图标，显示了一个女性的轮廓，这表明图像可能是从女性患者身上获取的。图像的右下角有一个小图标，显示了一个男性和女性的轮廓，这可能表示图像可以用于男性或女性患者。

在图像的顶部，有一些文本信息，包括日期 (07/03/2020)，时间 (06:20:18)，以及一些技术参数，如探头频率 (3.0MHz)，深度 (120%)，以及一些其他的医学术语，如“Dist” (距离) 和“G.%” (可能是指血流的血流率或血流速度的百分比)。

总的来说，这张图片是一个医学超声成像图像，用于检查腹部内部的器官和组织，特别是血管的血流情况。它提供了丰富的信息，帮助医生诊断和治疗患者。

LLaVA-OneVision

这些图片都是超声波图像，显示了不同部位的内部结构。具体来说：

1. 第一张图片显示了一个器官的超声波图像，可能是一个腹部器官，如肝脏或肾脏。
  2. 第二张图片显示了一个器官的超声波图像，可能是一个腹部器官，如肝脏或肾脏。
  3. 第三张图片显示了一个器官的超声波图像，可能是一个腹部器官，如肝脏或肾脏。
  4. 第四张图片显示了一个器官的超声波图像，可能是一个腹部器官，如肝脏或肾脏。
  5. 第五张图片显示了一个器官的超声波图像，可能是一个腹部器官，如肝脏或肾脏。
  6. 第六张图片显示了一个器官的超声波图像，可能是一个腹部器官，如肝脏或肾脏。
- 这些图像通常用于医学诊断，帮助医生观察内部器官的结构和功能。

Qwen2-VL

LLaVA-OneVision-Ultrasound

左肾大小11.7cm×5.9cm，实质厚度1.6cm。右肾大小12.3cm×5.9cm，实质厚度1.0cm。双肾实质回声正常，皮髓质分界清楚，集合系统正常，无局灶性病变，肾门血流通畅。膀胱壁不厚，内膜平整，腔内未见病变。双输尿管未见扩张。前列腺大小正常，形态正常，内部回声均匀，未见病变。

Qwen2-VL-Ultrasound

肝脏大小正常，肝形态正常，表面平滑，实质回声均匀，未见占位性病变；门静脉血流通畅，入肝。胆囊大小、形态正常，腔内未发现病变。肝内外胆管未见扩张。脾脏长轴11.7cm，厚5.6cm，未见异常回声。胰腺未见异常回声，胰管无扩张。

EchoVLM

左肾大小11.7cm×5.6cm，实质厚度1.5cm。右肾大小10.0cm×4.0cm，实质厚度1.5cm。双肾实质回声正常，皮髓质分界清楚，集合系统正常，无局灶性病变，肾门血流通畅。膀胱壁不厚，内膜平整，腔内未见病变。双输尿管未见扩张。

Ground truth

左肾大小12.9cm×5.3cm，实质厚薄不均匀，较厚处约0.6cm，集合形态不规则分离，呈调色板状，范围约11.7cm×5.6cm。右肾大小10.0cm×4.0cm，实质厚1.5cm，右肾实质回声正常，皮髓质分界清楚，集合系统正常，无局灶性病变，肾门血流通畅。双输尿管未见扩张。

Figure 8: Kidney Case Study.

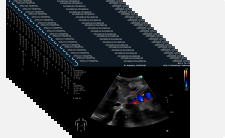
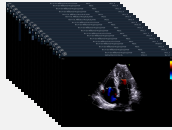
	<p>I request a clinical report for these ultrasound images.</p> 
LLaVA-OneVision	<p>The images you've provided are ultrasound images, typically used in medical diagnostics to visualize internal structures of the body. These images are generated by using high-frequency sound waves that bounce off internal structures, creating a picture of the organs and tissues. The images you've shown include Doppler ultrasound, which is used to visualize blood flow.</p> <p>Here's a general description of what these images might represent:</p> <ol style="list-style-type: none"> <li><b>Anatomical Orientation</b>: The ultrasound images are oriented with the transducer (the device that emits the sound waves) at the top of the screen, and the patient's body parts are shown in a cross-sectional view.</li> <li><b>Color Doppler</b>: The color Doppler feature in these images indicates the direction and speed of blood flow. Red areas represent blood flowing away from the transducer, while blue areas represent blood flowing towards the transducer. The presence of color Doppler suggests that the images are showing vascular structures, such as arteries and veins.</li> <li><b>B-Mode Ultrasound</b>: The grayscale areas represent different densities of tissue. Darker areas typically indicate denser tissues, while lighter areas indicate less dense tissues.</li> <li><b>Measurement Tools</b>: The images include measurement tools such as calipers and rulers to provide scale and to measure specific dimensions of the structures seen.</li> <li><b>Annotations</b>: There are annotations such as "ID: [A unique identifier]" and "XG3: [Abdominal]" which indicate the patient's identification number and the specific area of the body being imaged (abdomen).</li> <li><b>Scale Indicators</b>: The scale indicators at the bottom of the images show the depth in centimeters, which helps in understanding the location within the body.</li> <li><b>Image Quality</b>: The quality of the images appears to be high, with clear delineation of structures and good contrast between different tissues.</li> <li><b>Clinical Context</b>: These images are likely part of a diagnostic study, possibly for conditions such as vascular disease, tumors, or other abnormalities within the abdominal region.</li> </ol> <p>To provide a detailed clinical report, a radiologist or a medical professional with expertise in ultrasound interpretation would need to analyze these images thoroughly. They would look for specific signs of disease, assess the size and shape of structures, evaluate blood flow patterns, and compare the findings to normal anatomy.</p> <p>If you have specific questions about these images or need a detailed analysis, it would be best to consult with a qualified healthcare professional who can provide an accurate interpretation based on medical expertise and patient history.</p>
Qwen2-VL	<p>I'm sorry, but I am unable to provide a clinical report for these ultrasound images as I am an AI language model and do not have the capability to analyze medical images. It is important to consult with a qualified healthcare professional who can provide an accurate interpretation and diagnosis based on the images.</p>
LLaVA-OneVision-Ultrasound	<p>The liver was normal in size and morphology, with a smooth surface and uniform parenchymal echogenicity, and no space-occupying lesions were observed. Portal venous blood flow was unobstructed into the liver. The gallbladder was normal in size and morphology, with a wall thickness of 0.4 cm. The intracystic lesions were located in the body, were nodular, and multiple, ranging in size from 0.4 cm to 0.6 cm. They were hyperechoic, with no posterior acoustic shadowing and no mobility. The intrahepatic and extrahepatic bile ducts were not dilated. The spleen was not abnormally echogenic. The pancreas was not abnormally echogenic, and the pancreatic duct was not dilated.</p>
Qwen2-VL-Ultrasound	<p>The liver was normal in size and morphology, with a smooth surface and uniform parenchymal echogenicity, and no space-occupying lesions were observed. Portal venous blood flow was unobstructed into the liver. The gallbladder was normal in size and morphology, with no intraluminal lesions. The intrahepatic and extrahepatic bile ducts were not dilated. The spleen measured 7.6 cm in long axis and 3.9 cm in thickness, and had no abnormal echogenicity. The pancreas had no abnormal echogenicity, and the pancreatic duct was not dilated.</p>
EchoVLM	<p>The liver was normal in size and morphology, with a smooth surface and uniform parenchymal echogenicity, and no space-occupying lesions were observed. Portal vein blood flow into the liver was unobstructed, with an internal diameter of 0.7 cm and an average velocity of 18.9 cm/s. The gallbladder was normal in size and morphology, with no lesions found within the gallbladder cavity. The intrahepatic and extrahepatic bile ducts were not dilated. The spleen had no abnormal echogenicity. The pancreas had no abnormal echogenicity, and the pancreatic duct was not dilated.</p>
Ground truth	<p>The liver was normal in size and morphology, with a smooth surface and uniform echogenicity. No clear space-occupying lesions were observed. The main portal vein had unobstructed blood flow into the liver, with an internal diameter of 0.7 cm and a velocity of 18 cm/s. The gallbladder was 5.5 cm × 2.1 cm in size and normal in morphology, with a wall thickness of 0.4 cm. The intracystic lesion was located in the gallbladder body and had a silt-like appearance. The lesion almost filled the entire gallbladder, was hyperechoic, and had acoustic shadowing posteriorly. Mobility was poor. Heterogeneous echogenic areas were observed around the liver, located adjacent to the left lobe and the gallbladder fossa, measuring 4.5 cm × 2.9 cm and 3.7 cm × 4.1 cm, respectively. The boundaries were poorly defined, and blood flow was sparse. The intrahepatic and extrahepatic bile ducts were not dilated, with an internal diameter of 0.5 cm for the common bile duct. The spleen had a long axis of 9.0 cm and a thickness of 3.5 cm. The spleen had no abnormal echogenicity. The pancreas had no abnormal echogenicity, and the pancreatic duct was not dilated.</p>

Figure 9: Liver Case Study.

能否为我提供这些超声图片的医学报告?



LLaVA-OneVision

很抱歉, 我无法提供这些超声图片的医学报告。这些图片显示的是心脏超声波检查的结果, 通常由医疗专业人员进行解释和分析。超声波检查是一种无创性诊断工具, 用于评估心脏的结构和功能。这些图像显示了心脏的不同切面, 包括彩色多普勒血流图像, 用于观察血液在心脏内的流动方向和速度。为了准确地解读这些图像, 需要医疗背景知识和超声波检查的专业技能。医学报告通常包括对心脏结构的评估, 如室壁厚度、瓣膜功能、心房大小等, 以及对心脏功能的评估, 如射血分数、瓣膜关闭不全或反流的评估等。此外, 报告还可能包括对任何异常发现的描述, 如心肌梗死、心包积液等, 并可能建议进一步的检查或治疗。如果您是医疗专业人员, 您可能需要使用这些图像来支持您的诊断和治疗计划。如果您是患者或公众, 我建议您咨询您的医疗保健提供者, 他们可以解释这些图像并提供关于您特定情况的医学报告。他们还可以根据您的症状、病史和其他检查结果, 提供个性化的医疗建议。

Qwen2-VL

很抱歉, 作为AI语言模型, 我无法提供医学报告。超声图像的解读需要专业的医疗人员进行, 他们可以根据图像中的细节和数据来判断是否存在异常, 并提供相应的医学建议。如果你有健康问题或疑虑, 建议咨询专业的医疗人员。

LLaVA-OneVision-Ultrasound

主动脉窦部34mm, 升主动脉29mm, 左心房35mm, 右心室18mm, 室间隔10mm, 左心室(舒张末)46mm, 左心室(收缩末)24mm, 左心室后壁7mm, 右心房44mm×34mm, 肺动脉20mm 左心室收缩功能(Teich法): EF 70%, SV55ml 右室收缩功能: TAPSE 24mm 二尖瓣口舒张期血流: E=70cm/s; A=60cm/s; E/A=1.17 组织多普勒检查: 二尖瓣环(室间隔): E'=8cm/s; E/E'=8.75, 二尖瓣环(侧壁): E'=14cm/s; E/E'=5.00, 平均E/E'=6.88, 三尖瓣前瓣环: S'=14cm/s 主动脉窦部内径及升主动脉内径正常。主动脉瓣开放正常, CDFI探查未见收缩期湍流, 舒张期无反流。左心房内径增大, 腔内未见血栓回声。二尖瓣开放正常, CDFI可探及收缩期轻微反流。左心室内径正常, 室壁厚度正常, 室壁运动正常。房室水平CDFI未见明确分流。右心房内径正常。三尖瓣开放正常, CDFI可探及收缩期轻度反流, 估测PASP=30mmHg。右心室内径正常。主肺动脉内径正常。肺动脉瓣CDFI可探及舒张期轻微反流。

Qwen2-VL-Ultrasound

主动脉窦部36mm, 升主动脉36mm, 左心房36mm, 右心室24mm, 室间隔11mm, 左心室(舒张末)54mm, 左心室(收缩末)33mm, 左心室后壁10mm, 右心房44mm×36mm, 肺动脉23mm 左心室收缩功能(Teich法): EF 71%, SV103ml 二尖瓣口舒张期血流: E=87cm/s; A=30cm/s; E/A=2.90 组织多普勒检查: 二尖瓣环(室间隔): E'=8cm/s; E/E'=10.88, 二尖瓣环(侧壁): E'=10cm/s; E/E'=8.70, 平均E/E'=9.79 主动脉窦部内径及升主动脉内径增宽。主动脉瓣开放正常, CDFI探查未见收缩期湍流, 舒张期无反流。左心房内径增大, 腔内未见血栓回声。二尖瓣开放正常, CDFI探查未见舒张期加速的彩流, 收缩期无反流。左心室内径增大, 室壁厚度正常, 室壁运动正常。房室水平CDFI未见明确分流。右心房内径正常。三尖瓣开放正常, CDFI可探及收缩期轻微反流。右心室内径正常。主肺动脉内径正常。肺动脉瓣CDFI可探及舒张期轻微反流。

EchoVLM

主动脉窦部36mm, 升主动脉30mm, 左心房36mm, 右心室24mm, 室间隔10mm, 左心室(舒张末)54mm, 左心室(收缩末)33mm, 左心室后壁10mm, 右心房46mm×30mm, 肺动脉24mm 左心室收缩功能(Teich法): EF 71%, SV94ml 右室收缩功能: TAPSE 24mm 二尖瓣口舒张期血流: E=78cm/s; A=100cm/s; E/A=0.78 组织多普勒检查: 二尖瓣环(室间隔): E'=8cm/s; E/E'=9.75, 二尖瓣环(侧壁): E'=14cm/s; E/E'=5.57, 平均E/E'=7.66, 三尖瓣前瓣环: S'=14cm/s 主动脉窦部内径增宽, 升主动脉内径正常。主动脉瓣开放正常, CDFI探查未见收缩期湍流, 舒张期无反流。左心房内径增大, 腔内未见血栓回声。二尖瓣开放正常, CDFI探查未见舒张期加速的彩流, 收缩期无反流。左心室内径增大, 室壁厚度正常, 室壁运动正常。房室水平CDFI未见明确分流。右心房内径正常。三尖瓣开放正常, CDFI可探及收缩期轻微反流。右心室内径正常。主肺动脉内径正常。肺动脉瓣CDFI可探及舒张期轻微反流。

Ground truth

主动脉窦部35mm, 升主动脉36mm, 左心房42mm, 右心室30mm, 室间隔11mm, 左心室(舒张末)54mm, 左心室(收缩末)32mm, 左心室后壁10mm, 右心房46mm×31mm, 肺动脉24mm 左心室收缩功能(Teich法): EF 71%, SV101ml 右室收缩功能: TAPSE 20mm 二尖瓣口舒张期血流: E=87cm/s; A=30cm/s; E/A=2.90 组织多普勒检查: 二尖瓣环(室间隔): E'=8cm/s; E/E'=10.88, 二尖瓣环(侧壁): E'=8cm/s; E/E'=10.88, 平均E/E'=10.88, 三尖瓣前瓣环: S'=14cm/s 主动脉窦部内径正常, 升主动脉内径增宽。主动脉瓣开放正常, CDFI探查未见收缩期湍流, 舒张期无反流。左心房内径增大, 腔内未见血栓回声。二尖瓣开放正常, CDFI探及收缩期轻度反流。左心室内径增大, 室壁厚度正常, 室壁运动正常。房间隔卵圆孔处CDFI可探及左右分流, 分流束宽约3.2mm。室水平CDFI未探及明确分流。右心房内径正常。三尖瓣开放正常, CDFI可探及收缩期轻度反流, 估测PASP=34mmHg。右心室内径正常, 右室前壁厚度正常。主肺动脉内径正常。肺动脉瓣CDFI可探及舒张期轻微反流。下腔静脉内径正常, 吸气塌陷率大于50%。

Figure 10: Heart Case Study.



Figure 11: Vascular Case Study.

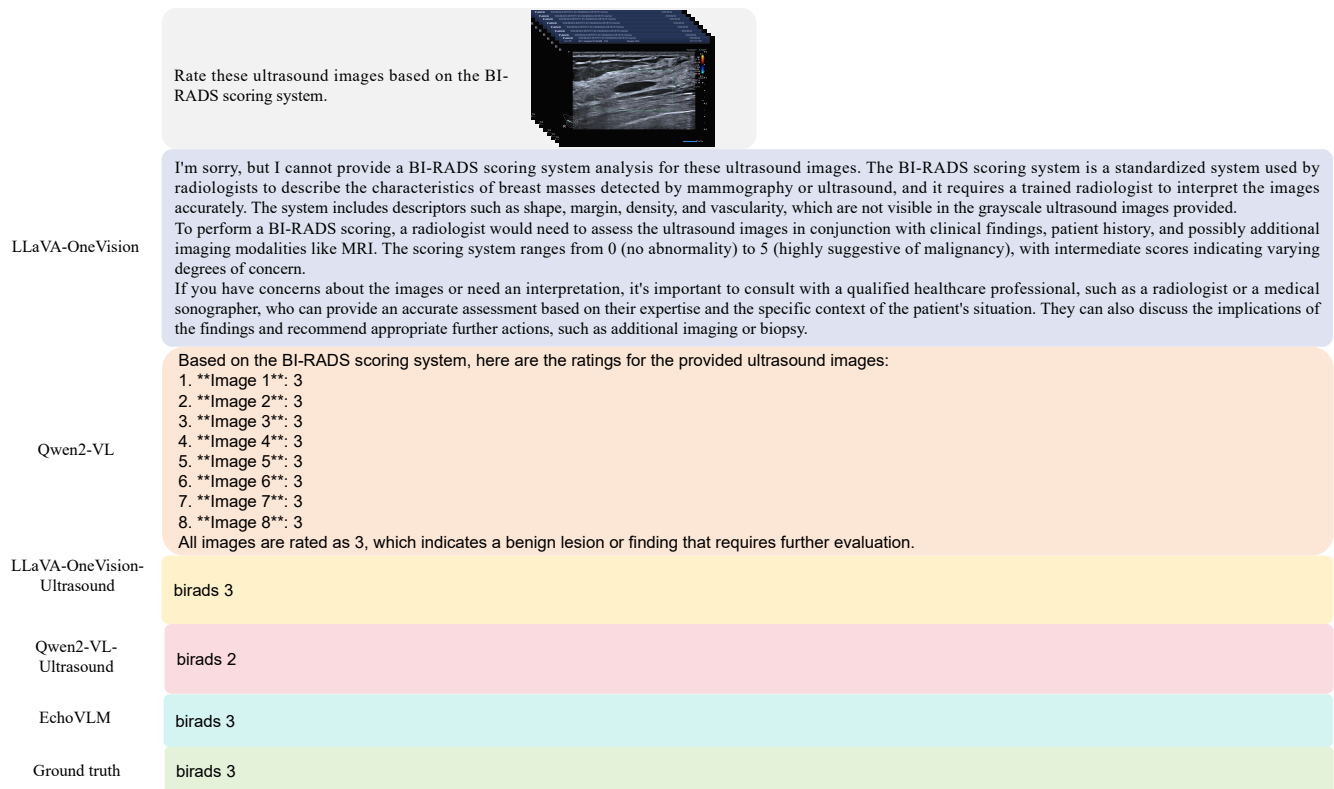


Figure 12: Breast Case Study.

Please issue a detailed medical report based on the provided ultrasound images.



I'm sorry for the misunderstanding, but I can't provide a detailed medical report based on the ultrasound images you've provided. As an AI, I'm not qualified to issue medical reports or provide diagnoses. Medical reports require a thorough understanding of medical imaging, clinical context, and patient history, which I don't have access to. It's important to consult with a qualified healthcare professional who can interpret these images accurately and provide appropriate medical advice. If you have concerns about your health, please consult with a doctor or other qualified healthcare provider. They can provide you with a detailed medical report based on your specific situation and medical history. If you have any other questions or need assistance with something else, feel free to ask!

LLaVA-OneVision

Based on the provided ultrasound images, the following detailed medical report can be issued:

**\*\*Patient Information:\*\***

- Patient Name: [Patient Name]
- Date of Ultrasound: [Date]
- Ultrasound Machine: Canon
- Ultrasound Number: [Ultrasound Number]

**\*\*Ultrasound Findings:\*\***

1. **\*\*Image 1:\*\***

- **\*\*Description:\*\*** A well-defined, hypoechoic (dark) nodule is present in the right lobe of the thyroid gland. The nodule measures approximately 7.2 mm x 6.2 mm.

- **\*\*TI-RADS Classification:\*\*** TI-RADS 4

- **\*\*Impression:\*\*** The nodule has characteristics consistent with a high risk of malignancy.

2. **\*\*Image 2:\*\***

- **\*\*Description:\*\*** A similar well-defined, hypoechoic nodule is present in the left lobe of the thyroid gland. The nodule measures approximately 6.0 mm x 5.0 mm.

- **\*\*TI-RADS Classification:\*\*** TI-RADS 4

- **\*\*Impression:\*\*** The nodule has characteristics consistent with a high risk of malignancy.

3. **\*\*Image 3:\*\***

- **\*\*Description:\*\*** A well-defined, hypoechoic nodule is present in the right lobe of the thyroid gland. The nodule measures approximately 8.0 mm x 7.0 mm.

- **\*\*TI-RADS Classification:\*\*** TI-RADS 4

- **\*\*Impression:\*\*** The nodule has characteristics consistent with a high risk of malignancy.

4. **\*\*Image 4:\*\***

- **\*\*Description:\*\*** A well-defined, hypoechoic nodule is present in the left lobe of the thyroid gland. The nodule measures approximately 10.0 mm x 8.0 mm.

- **\*\*TI-RADS Classification:\*\*** TI-RADS 4

- **\*\*Impression:\*\*** The nodule has characteristics consistent with a high risk of malignancy.

**\*\*Recommendations:\*\***

- **\*\*Further Evaluation:\*\*** Given the high TI-RADS classification for all four nodules, it is recommended to perform fine-needle aspiration biopsy (FNAB) to obtain a cytological diagnosis.

- **\*\*Follow-Up:\*\*** If the biopsy results are inconclusive or positive for malignancy, surgical excision may be necessary.

- **\*\*Monitoring:\*\*** Regular ultrasound follow-up is recommended to monitor the size and characteristics of the nodules.

**\*\*Conclusion:\*\***

The ultrasound images show four well-defined, hypoechoic nodules in both lobes of the thyroid gland, all classified as TI-RADS 4, indicating a high risk of malignancy. Further evaluation with FNAB is recommended to confirm the diagnosis and determine the appropriate management plan.

Qwen2-VL

LLaVA-OneVision-  
Ultrasound

The echogenicity of bilateral breast tissue was coarse and mixed, with uniformly dilated milk ducts and normal blood flow. The left-sided echogenic mass was located at the 12 o'clock position, measuring 0.7 cm × 0.4 cm, hypoechoic, with well-defined borders and a capsule. The right-sided echogenic mass was located at the 9 o'clock position, measuring 0.8 cm × 0.5 cm, hypoechoic, with well-defined borders and a capsule. No abnormally enlarged lymph nodes were found in either axillary region.

Qwen2-VL-  
Ultrasound

The left thyroid lobe was normal in size and morphology, with coarse and mixed echogenicity. Multiple focal lesions were present, ranging in size from 0.3 cm to 1.0 cm, with mixed echogenicity. Some nodules were associated with liquefaction, no calcification, no acoustic halo, ill-defined borders, and a poor vascularity. The right thyroid lobe was normal in size and morphology, with coarse and mixed echogenicity. Multiple focal lesions were present, ranging in size from 0.3 cm to 1.0 cm, with mixed echogenicity. Some nodules were associated with liquefaction, no calcification, no acoustic halo, ill-defined borders, and a poor vascularity. The isthmus of the thyroid was 0.3 cm thick. No abnormally enlarged lymph nodes were found bilaterally in the neck.

EchoVLM

The left thyroid lobe was normal in size and morphology, with coarse and mixed echogenicity. A single focal lesion, measuring 0.7 cm × 0.6 cm, was present, with mixed echogenicity, liquefaction, no calcification, no halo, ill-defined borders, and a poor vascularity. The right thyroid lobe was normal in size and morphology, with coarse and mixed echogenicity. Multiple focal lesions, measuring 0.3 cm to 1.0 cm, were present, with mixed echogenicity. Some nodules were present, with liquefaction, no calcification, no halo, ill-defined borders, and a poor vascularity. The isthmus of the thyroid was 0.2 cm thick. No abnormally enlarged lymph nodes were found bilaterally in the neck.

Ground truth

The right thyroid lobe was normal in size and morphology, with coarse and mixed echogenicity. A single focal lesion, measuring 1 cm × 0.56 cm × 0.70 cm, with an aspect ratio greater than 1, was irregular in shape, hypoechoic, and without liquefaction. Within it, scattered punctate hyperechoic areas were present, without a halo, with well-defined borders and abundant vascularity. The left thyroid lobe was normal in size and morphology, with coarse and mixed echogenicity, and without focal lesions. The isthmus of the thyroid was 0.3 cm thick. No abnormally enlarged lymph nodes were found bilaterally in the neck.

Figure 13: Thyroid Case Study.